Geochimica et Cosmochimica Acta 368 (2024) 93–111

Contents lists available at ScienceDirect

Geochimica et Cosmochimica Acta

journal homepage: www.elsevier.com/locate/gca

High CO_2 in the mantle source of ocean island basanites

Francesco Maria Lo Forte [a,*], Federica Schiavi [b], Estelle F. Rose-Koga [c], Silvio G. Rotolo [a,d], Maximilien Verdier-Paoletti [e], Alessandro Aiuppa [a], Vittorio Zanon [f]

[a] Dipartimento di Scienze della Terra e del Mare, Università degli Studi di Palermo, Palermo 90123, Italy
[b] Université Clermont Auvergne, CNRS, IRD, OPGC, Laboratoire Magmas et Volcans, F-63000 Clermont-Ferrand, France
[c] Institut des Sciences de la Terre d'Orléans (ISTO) UMR 7327, CNRS-Université d'Orléans-BRGM, 1A rue de la Férollerie, 45071 Orléans, Cedex 2, France
[d] Istituto Nazionale di Geofisica e Vulcanologia, Sezione di Palermo, Via Ugo La Malfa 153, 90146 Palermo, Italy
[e] Muséum National d'Histoire Naturelle de Paris (MNHN), Institut de Minéralogie, de Physique des Matériaux, 61 rue Buffon CP52, 75005 Paris, France
[f] Instuto de Investigação em Vulcanologia e Avaliação de Riscos, Universidade dos Açores, Rua Mãe de Deus, Ponta Delgada 9501-801, Portugal

ARTICLE INFO

Associate editor: Andreas Stracke

Keywords:
Alkaline ocean islands
Intraplate volcanism
Fogo volcano
Melt inclusions
Cape Verde

ABSTRACT

Some of the most CO_2-rich magmas on Earth are erupted by intraplate ocean island volcanoes. Here, we characterise olivine-hosted melt inclusions from recent (<10 ky) basanitic tephra erupted by Fogo, the only active volcano of the Cape Verde Archipelago in the eastern Atlantic Ocean. We determine H_2O, S, Cl, F in glassy melt inclusions and recalculate the total (glass + shrinkage bubbles) CO_2 budget by three independent methodologies. We find that the Fogo parental basanite, entrapped as melt inclusion in forsterite-rich (Fo_{80-85}) olivines, contains up to ~2.1 wt% CO_2, 3–47 % of which is partitioned in the shrinkage bubbles. This CO_2 content is among the highest ever measured in melt inclusions in OIBs. In combination with ~2 wt% H_2O content, our data constrain an entrapment pressure range for the most CO_2-rich melt inclusion of 648–1430 MPa, with a most conservative estimate at 773–1020 MPa. Our results therefore suggest the parental Fogo melt is stored in the lithospheric mantle at minimum depths of ~27 to ~36 km, and then injected into a vertically stacked magma ponding system. Overall, our results corroborate previous indications for a CO_2-rich nature of alkaline ocean island volcanism. We propose that the Fogo basanitic melt forms by low degrees of melting (F = 0.06–0.07) of a carbon-enriched mantle source, containing up to 355–414 ppm C. If global OIB melts are dominantly as carbon-rich as our Fogo results suggest, then OIB volcanism may cumulatively outgas as high as ~16–21 Tg of carbon yearly, hence substantially contributing to the global deep carbon cycle.

1. Introduction

Quantifying the initial amount of volatile elements (H_2O, CO_2, S, Cl, and F) transported by OIB magmas is essential for understanding the cycling of volatiles from Earth's deep interior (e.g., Hirschmann, 2006, 2018; Dasgupta and Hirschmann, 2010), and their role for mantle melting, and magma generation and extraction (e.g., Foley, 2011; Dasgupta, 2018). Although sustaining only ~10 % of the annual magma output on Earth, OIB magmas can contain more than 5 % volatiles, and therefore significantly contribute to the annual magmatic gas output (e.g., Cabral et al., 2014; Longpré et al., 2017; Boudoire et al., 2018; Taracsák et al., 2019; Burton et al., 2023), especially if compared to more voluminous - but less volatile rich - Mid Ocean Ridge Basalts (MORBs) (e.g., Hauri et al., 2019). Oceanic intra-plate magmas have some of the most CO_2-enriched magmas on Earth (Longpré et al., 2017; Taracsák et al., 2019), likely reflecting their derivation from low melting degree of a metasomatised (C-enriched) mantle source (Foley et al., 2009, 2011; Dasgupta et al., 2013; Foley and Fischer, 2017; Dasgupta, 2018; Aiuppa et al., 2021).

Glassy melt inclusions (MI), small droplets of silicate melt entrapped in crystals during their growth in magmas or during episodes of crystal fracturing, are - at least in principle - physically and chemically isolated systems shielded from the surrounding environment by the host crystal (e.g., Lowenstern 1995; Danyushevsky et al., 2002; Schiano, 2003; Wallace, 2005; Cannatelli et al., 2016; Wallace et al., 2021; Rose-Koga et al., 2021). As such, the entrapped melt should escape extensive volatile loss upon magma ascent/storage in the crust prior/during eruption. Upon quenching as glass, MI should allow recording the dissolved volatile contents at the P-T-X conditions of entrapment, and eventually the parental melt volatile contents if entrapment has occurred at/near

* Corresponding author.
E-mail address: francescomaria.loforte@unipa.it (F.M. Lo Forte).

https://doi.org/10.1016/j.gca.2024.01.016
Received 28 August 2023; Accepted 17 January 2024
Available online 26 January 2024

source (and before volatile saturation is reached) (e.g., Métrich and Wallace, 2008; Edmonds and Wallace, 2017). However, the task is complicated by a range of processes that can potentially modify MI composition after it is entrapped in the crystal (e.g., Anderson, 1974; Roedder, 1979; Danyushevsky et al., 2002; Wallace et al., 2021), including post-entrapment crystallization at the MI-host crystal interface (e.g., Danyushevsky et al., 2000), diffusive exchanges of major, trace and volatile (H^+) elements (e.g., Gaetani and Watson, 2000, 2002; Danyushevsky, 2001; Cottrell et al., 2002; Gaetani et al., 2012) and – above all – shrinkage bubble formation (Anderson, 1974; Roedder, 1979; Maclennan, 2017). This latter process is especially relevant for volatile species, as it leads to partitioning of poorly soluble CO_2 from the melt inclusion glass into the shrinkage bubble. Shrinkage bubbles can contain up to > 90 % of the bulk MI CO_2 content (e.g., Mironov and Portnyagin, 2011; Hartley et al., 2014; Mironov et al., 2015; Moore et al., 2015; Esposito et al., 2016; Aster et al., 2016; Rasmussen et al., 2018, 2020), demonstrating the caveats of traditional approaches (Lowenstern, 2015) that focus on measuring volatiles in glass only. Still, accurately quantifying the shrinkage bubble CO_2 content is technically challenging (e.g., Naumov et al., 2003), and few examples are available of reconstructions of the total (bubble + glass) MI CO_2 budget in OIB (e.g., Taracsák et al., 2019; Tucker et al., 2019, Burton et al., 2023).

Some of the most alkali-rich OIB magmas are erupted in the Cape Verde Archipelago, in the central eastern Atlantic. This archipelago lies on the largest intraplate bathymetric anomaly in the Earth's oceans – the Cape Verde Rise - interpreted as the surface expression of a hotspot sustained by the ascent of a deeply-rooted mantle plume (Holm et al., 2006; French and Romanowicz, 2015). The presence of highly alkaline silica undersaturated rocks (nephelinites, melanephelinites, and melilitites), as well as carbonatites (Hoernle et al., 2002; Bonadiman et al., 2005), are evidence for a heterogeneous, oxidized (Moussallam et al., 2019), potentially C-enriched mantle source, as also indicated by the CO_2-rich signature of fumaroles (Aiuppa et al., 2020; Melián et al., 2021).

In this study we use primitive MI composition to confirm the carbon-rich signature of the Cape Verde magma source. We report on the major, trace, and volatile composition of olivine-hosted MI from basanitic tephra erupted at Fogo, the youngest active volcano of the Cape Verde Archipelago. Our goal is to determine the initial (parental melt) volatile contents, in the attempt to (i) test the carbon-enriched source hypothesis, (ii) refine our understanding of the architecture of the magma system, and (iii) more broadly, provide additional evidence for the carbon-enriched nature of alkali rich, OIB magmatism. Our results are complementary to those recently reported by DeVitre et al. (2023) on similar suite of MI.

2. Volcanological background

Fogo is the only active volcano in the Cape Verde Archipelago, in the central eastern Atlantic (Fig. 1). Volcanic activity on the islands started ~26 Ma (Torres et al., 2010), and is dominated by silica-undersaturated alkaline melts (e.g., Gerlach et al., 1988), and rarer carbonatites (Hoernle et al., 2002; Mourão et al., 2012). Subaerial volcanic activity has been divided into four eruptive phases: (i) The Ribeira de Almada Group (~4.5 Ma, Foeken et al., 2009); (ii) The Monte Barro Group (of unknown age); (iii) The Monte Amarelo Group, whose activity preceded the lateral collapse of Monte Amarelo at circa 62 to 123 ka (Day et al., 1999; Foeken et al., 2009; Martínez-Moreno et al., 2018); and (iv) The

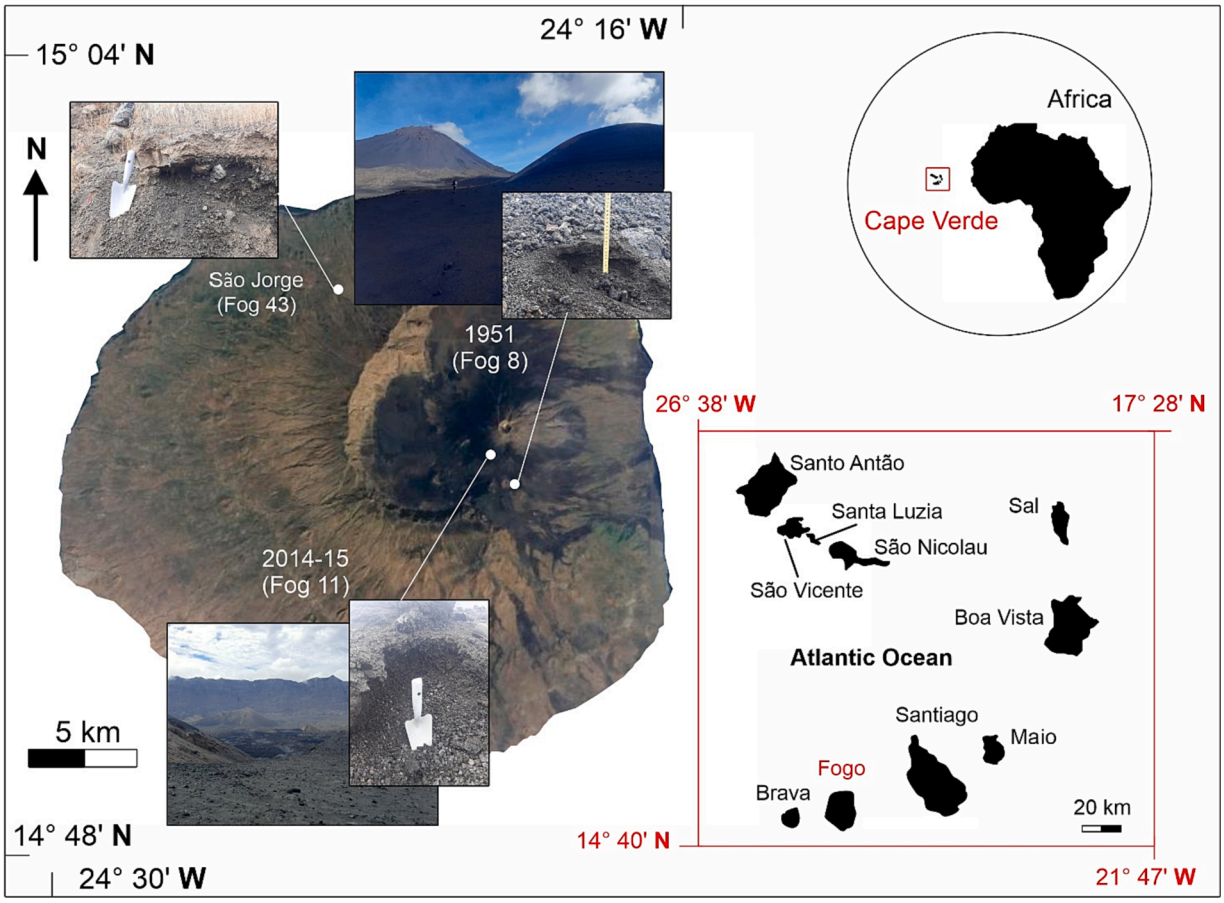

Fig. 1. Modified Satellite map of Fogo Island from Google Earth, showing sampling sites with their relative pictures. Insets show the location of the Cape Verde archipelago (top right), and Fogo Island (bottom right).

Chã das Caldeira Group (Foeken et al., 2009) related to the recent growth of Pico do Fogo central volcano. The Pico do Fogo volcano erupted 28 times since the 1500 s. Eruptions are sourced by a complex, vertically elongated magma plumbing system, with main magma storage/stagnation zones at~24,~13-19 and~9-12 km depth (Hildner et al., 2011, 2012; Klügel et al., 2020; Lo Forte et al., 2023).

3. Materials and methods

3.1. Sample preparation

We report data for 18 MI hosted in 12 olivine phenocrysts from three different tephra samples representative the last eruptive phase of Fogo volcano (see tables S1 and S2 of Supplementary Material S1, for further details). In detail, we analysed (i) 8 MI hosted in 5 olivines from the clinopyroxene- and olivine-rich tephra samples of São Jorge (SJ), of the early Holocene period of activity (10 ka), and (ii) 10 MI hosted in 7 olivines from the recent basanitic tephra samples of the 1951 and 2014/15 eruptions. Samples were prepared according to the methodology described by Rose-Koga et al., (2021). Tephra samples were initially sieved to separate grain size populations in the 250–4000 μm range. For each sample, about 400 olivine phenocrysts were hand-picked from these grain size fractions. Olivine crystals were mounted on glass slides using Crystal Bond 509®, subsequently they were doubly polished with silicon carbide paper and alumina powders to attain a maximum thickness of 80–100 μm. Twenty phenocrysts, containing 26 MIs with size greater than 25 μm were selected for analysis.

3.2. Analytical techniques

Electron microprobe analysis (EMPA) was used to determine the major element compositions of both host olivines and melt inclusions, as well as Cl, and F concentrations in glasses. Volatile element concentrations (H_2O, CO_2, S, and Cl) in glasses were measured by nano-SIMS. The CO_2 concentration in shrinkage bubbles in MI was determined by Raman micro-spectroscopy. Finally, Laser Ablation-ICPMS was utilized for trace element analysis. The full compositional dataset is listed in tables S3, S4, S5, S5.1, and S5.2 of Supplementary Material S1.

3.2.1. Electron microprobe analysis

Electron microprobe analyses were performed with a Cameca SxFiveTactis with a LaB6 source equipped with five wavelength-dispersive spectrometers at the Laboratoire Magmas et Volcans (LMV), in Clermont-Ferrand, France. Major elements and volatiles were analysed in the same analytical session, with an accelerating voltage of 15 kV, an 8nA beam current, and a 20 μm defocused beam for major elements. Chlorine, sulphur, and fluorine analyses were conducted using an accelerating voltage of 15 kV, a 40nA beam current and a 20 μm defocused beam, following the acquisition program outlined in the Cameca Peak Sight software (see Rose-Koga et al., 2020 for more details). The olivines were analysed with an accelerating voltage of 15 kV and 15nA beam current. The total concentration of volatiles was determined by summing the counts from multiple iterations. Total counting times were 100 s for F and Cl peaks. The detection limits for F and Cl were 300 and 150 ppm, respectively. KE12 LMV, CFA47 (Spilliaert et al., 2006), and ALV-98I R23 glasses and the San Carlos olivine were used as standards. Typical errors on the samples (1σ error of mean) are less than 10 % for all elements analysed both in MI and in olivines.

3.2.2. Nano-SIMS analysis

High spatial resolution measurements of volatiles in minor and trace amounts in MI were conducted using the CAMECA nanoSIMS50 of the Muséum National d'Histoire Naturelle de Paris. All measurements were carried using a focussed Cs^+ primary ion beam accelerated to 16 keV in high vacuum conditions ($<8x10^{-10}$ mbar). Prior to acquisition, a 5 × 5 μm2 region was pre-sputtered with a 280 pA primary beam for 2 min to remove the Au coat and ensure a clean surface. The current was then reduced to 20 pA and the inner 3 × 3 μm2 were rastered over a 32 × 32 pixels matrix with a 1 ms/px dwell time during 100 cycles (~2 min). A numerical blanking was applied to 32 × 32 px matrix to consider only the innermost 1 × 1 μm2 region, this in order to limit the contribution of potential contamination. A cloud of electron was generated above the sample's surface to avoid the accumulation of positive charges induced by the implantation of the Cs^+ beam. ^{12}C, $^{16}O^1H$, ^{28}Si, ^{32}S, and ^{35}Cl were acquired simultaneously in multicollection mode on 5 electron multipliers (Ems). Each measurement was corrected for the 44 ns of the detector's deadtime. We used a 20 × 140 μm entrance slit (#3) with a 200 μm diameter aperture slit (#2) and a 10 % energy slit to optimize the Mass-Resolving Power (MRP) without compromising our transmission. This setting enabled a MRP > 8000 which ensured the separation of $^{16}O^1H$ and its isobaric interference ^{17}O. The standards used for the calibration of the different elements were: two glasses NIST 610 and 612; a Suprasil crystal; two basaltic glasses MRN-G1 and IND-G2 (Shimizu et al., 2017) and three internal standards STR 10–11-13 (Créon et al., 2018). All of this enables to achieve a statistically robust linear regression spanning a range of concentrations from wt% (H_2O) to hundreds of ppm (CO_2, S, Cl) (Figure S1 in the Supplementary Material S2). The nano-SIMS technique is typically associated with higher analytical precision (<5%) and lower detection limits (<10 ppm typically) for Cl (Rose-Koga et al., 2021) relative to electron probe (Rose-Koga et al., 2020). The Suprasil standards is a synthetic crystal known for its purity. It has been extensively used alongside Herasil crystal to assess the blank values for H_2O and CO_2 (e.g., Shimizu et al., 2021). By setting their concentrations at 0 in our calibrations we systematically subtract these blank contributions. Errors were estimated as the quadratic sum of the measured 1σ Poisson ratio error and the 1σ prediction/confidence interval local estimation and were subsequently reported as 2σ errors. For each measurement corrected by our determined linear regression we can extract an error associated with the estimation through the 95 % confidence interval. This error is then quadratically added to the error on the measurement itself (poissonian error on ratios).

3.2.3. Raman spectroscopy

Raman spectra were collected using an inVia confocal Raman microspectrometer manufactured by Renishaw and equipped with a 532.1 ± 0.3 nm diode-pulsed solid state laser (200 mW output power), a Peltier-cooled CCD detector of 1040 × 256 pixels, and a Leica DM 2500 M optical microscope with a motorised XYZ stage, at the LMV. Scattered light was collected via a back-scattered geometry. Laser power was about 10 mW on the sample surface. A 100x microscope objective, a grating of 2400 grooves mm^{-1}, and a 20-μm slit aperture (high confocality setting) were used, which resulted in spectral resolution better than 0.4 cm^{-1} and in vertical and horizontal spatial resolutions of approximately 2–3 and 1 μm, respectively, near the surface of the sample. Calibration of peak positions was performed at room temperature, based on the 520.5 cm^{-1} peak of silicon and the 1331.5 cm^{-1} peak of a diamond standard; two Neon emission bands of 568.98163 and 576.44188 nm wavelengths were used to check the linearity of the spectrometer. For CO_2 measurements in MI bubbles, the spectra were recorded from 725 to 1880 cm^{-1} using the WiRE™ 4.4 software. Then, spectra were acquired in the 60–1320 cm^{-1} wavenumber range to detect presence of mineral phases (e.g., carbonates, sulphates) or fluid SO_2. Finally, spectra were collected in the 2800–3900 cm^{-1} region to detect H_2O and/or OH^- molecules. Acquisition time for a single CO_2 analysis was fixed at 60 s. Spectra were initially treated for removal of cosmic rays, and then an appropriate polynomial baseline correction was applied before fitting a combined Gaussian-Lorentzian curve to the CO_2 Fermi diad (e.g., Moore et al., 2015; Mironov et al., 2020; Schiavi et al., 2020). The analytical uncertainty associated with CO_2 density measurements is < 0.05 g/cm^3 (Boudoire et al., 2023). Examples of Raman spectra acquired on shrinkage bubbles in melt inclusion are shown in

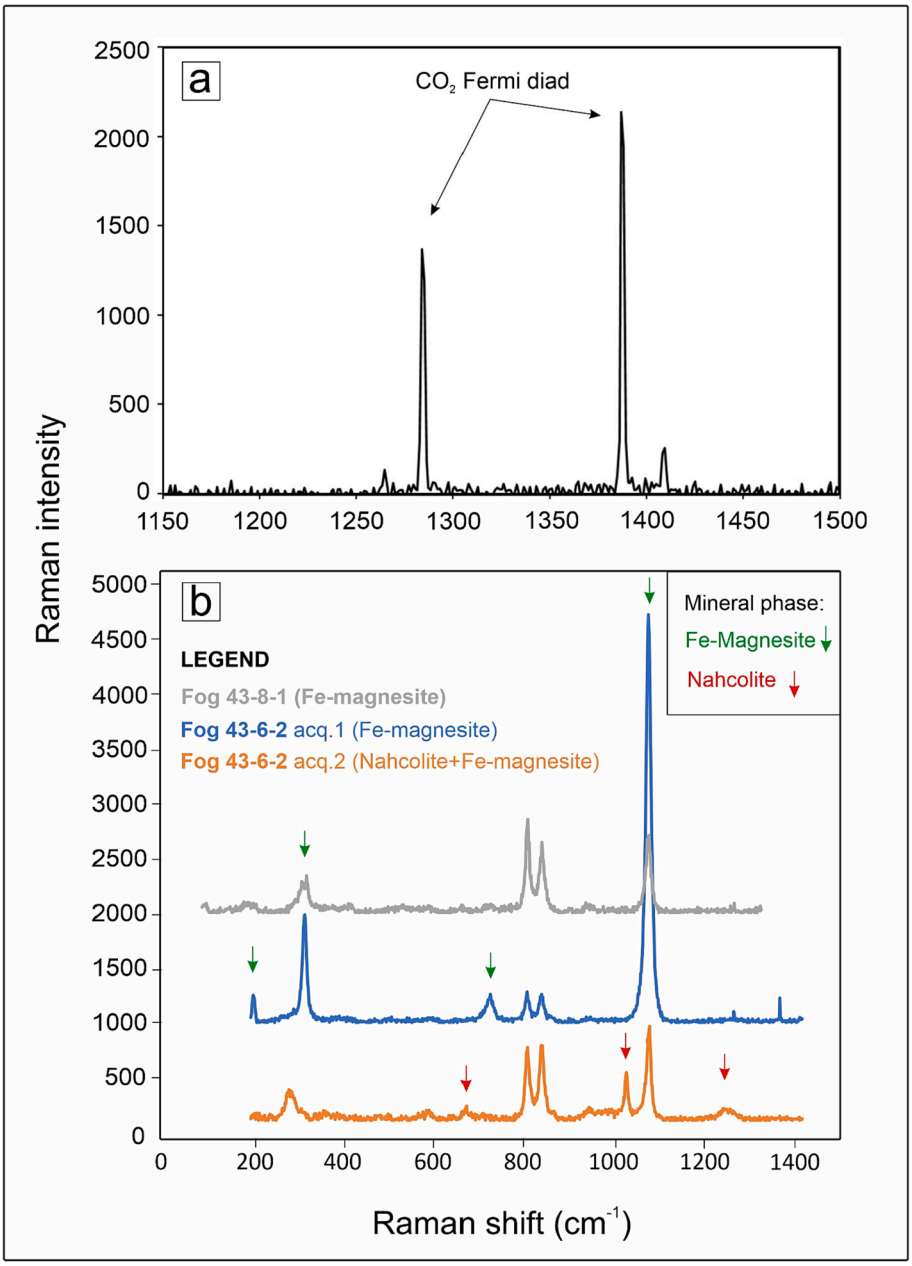

Fig. 2. (a) Raman spectrum of melt inclusion shrinkage bubble (sample Fog 43–8-1). The bubble is made of pure CO_2, as revealed by the two strong peaks at 1284 and 1387 cm^{-1}, identified as Fermi diad (Kawakami et al., 2003). The separation between the two Raman bands of CO_2 is a reliable densimeter for the CO_2 fluid. (b) Raman spectra collected from the shrinkage bubble of Fog 43–8-1 (grey spectrum) and Fog 43–6-2 (orange and light blue spectra, acquired during tomographic analysis) MI samples. In the bubble, minerals such as Fe-magnesite and nahcolite were identified, as evidenced by peaks at 318, 737, and 1092 cm^{-1} for Fe-magnesite, (Mg,Fe)CO_3 (Boulard et al., 2012) and the peaks at 685, 1045, and 1266 cm^{-1} for nahcolite, $NaHCO_3$ (Fall et al., 2007). Both spectra also exhibit the characteristic olivine peaks at~ 822 e 854 cm^{-1}.

Fig. 2. In all shrinkage bubbles, only CO_2 was detected as fluid phase (Fig. 2a).

3.2.4. *Laser ablation-ICPMS*

Trace-element measurements on melt inclusions were carried out using a laser ablation system (193 nm Excimer Resonetics M−50E) associated with an inductively coupled plasma mass spectrometer (Agilent 7500 cs LA–ICP–MS at the LMV). Analysis was performed following procedures outlined in the previous studies (e.g., Rose-Koga et al., 2012). We used a pulse energy of about 3 mJ, a spot diameter between 15 and 33 μm, and a laser pulse frequency of 2–3 Hz, depending in the inclusion size to keep a fluence at sample surface of about 4 J/cm^{-2}. The background was measured for 30–40 s before ablation and analysis time was approximately 100 s. Data reduction was performed using the GLITTER software (Van Achterbergh et al., 2001). This technique uses CaO (measured by electron probe) as an internal standard. Reproducibility and accuracy of the analysis were constrained by systematic analysis of two standards BCR2-G and SRM NIST 612 at the beginning, in the middle and at the end of the session. Typical errors on the samples (1σ error of mean) are less than 10 % for all trace elements analysed.

4. Results

4.1. Whole-rock and mineral chemistry

The studied tephra samples are nepheline-normative (Ne = 17.6–21.2 wt%) basanites (SiO_2 = 41.73–43.78 wt%; $K_2O + Na_2O$ = 6.69–7.68 wt%) (table 1 of Supplementary Data S1), with a common mineral assemblage represented by clinopyroxene, olivine, plagioclase, and Fe-Ti oxides. These tephra samples are part of the same suite analysed (for major elements and fluid inclusions) by Lo Forte et al. (2023). The olivine grains have euhedral shapes and exhibit a narrow range of compositions (forsterite mol% Fo_{80-85}) (table S3 of Supplementary Material S1). The olivine phenocrysts of sample SJ (Fog 43) are slightly more forsteritic (Fo_{83-85}) than the 1951 (Fog 8) and 2014/15 (Fog 11) olivines (Fo_{80-84}). The same SJ olivines exhibit higher CaO (0.34–0.40 wt%) and NiO (0.13–0.15 wt%) contents than the 1951 and 2014/2015 olivines (CaO, 0.31–0.39 wt%; NiO, 0.03–0.15 wt%). Mineral chemistry results are detailed in table S3 of Supplementary Material S1.

4.2. Melt inclusions: size and morphology

Olivines contain abundant MI, but only 13 % of them were large enough (>25 μm) for trace element analyses. All studied inclusions are perfectly glassy, and elliptical in shape (Fig. 3), with the long axis (a) ranging between 17.0 μm and 94.0 μm (mean, 49.6 μm) and the short axis (b) between 11.3 μm and 83.1 μm (mean, 40.7 μm). Different criteria are used in the literature to determine the size of the third semi-axis c (e.g., axis a > b = c, Hauri et al., 2018; Shaw et al., 2008, 2010; Wanless et al., 2014, 2015; geometric mean, Ni et al., 2017); direct measurements can be used to test different assumptions (Mironov et al., 2020). Here we use the criteria of Moore et al. (2015) that assumes axis (c) equals to the arithmetic mean of axes (a) and (b) of the ellipsoid. The semi-axis (c) is therefore estimated at between 14.2 μm and 88.5 μm (mean, 37.8 μm). Shrinkage bubbles were observed inside all the MI (table S7 of Supplementary Material S1). However, in 31 % of the selected MI the bubbles were lost during the polishing process as the MI surface was exposed for analysis. The MI in which bubbles were lost are not considered further (except samples Fog 43–3-1 for which we report glass CO_2 contents only). There is no textural evidence of MI decrepitation. Roughly half of the shrinkage bubbles contain mineral phases such as Fe-magnesite, nahcolite, and sulphates (Fig. 2b).

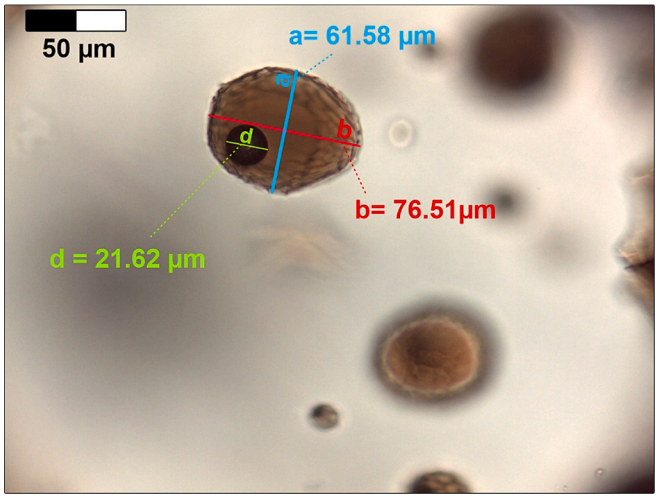

Fig. 3. Measurements of the major (a) and minor (b) axes of the MI (Fog 43–6-3) for the determination of the melt volume and measurement of the diameter (d) of the shrinkage bubble for the calculation of its volume.

4.3. Melt inclusion major element compositions and post-entrapment correction (PEC)

Melt inclusion glasses are foiditic to basanitic and compositionally overlap with bulk rocks (Fig. 4a). They typically contain 39.89–45.95 wt % SiO_2, 3.15–5.85 wt% MgO, 3.13–5.32 wt% Na_2O, and 8.07–10.74 wt % FeO_t (Fig. 4). A variety of processes may alter the melt composition after entrapment (see review in Wallace et al., 2021), including: (i) post-entrapment crystallization (PEC) of olivine at the MI-host mineral interface during slow cooling (Kent, 2008); (ii) volatile loss from the melt to the shrinkage bubbles (Wallace et al., 2015) or due to inclusion decrepitation (e.g., Maclennan, 2017); (iii) hydrogen ('water') diffusive loss (Hauri, 2002; Massare et al., 2002; Portnyagin et al., 2008, 2019; Chen et al., 2011; Gaetani et al., 2012); (iv) iron, magnesium diffusive exchange between the inclusion and its host mineral (e.g., Danyushevsky et al., 2000; Cottrell et al., 2002; Gaetani and Watson, 2000, 2002). We correct the composition of olivine-hosted MI for PEC using Melt inclusion modification corrections (MIMiC) (Rasmussen et al., 2020). The code employs the (KD^{Fe-Mg}) model of Toplis (2005) and the olivine-melt thermometer of Putirka et al. (2007) to calculate the Fe-Mg olivine-melt partitioning (at redox conditions estimated by Moussallam et al., 2019) and to estimate magma temperature, respectively. Melt inclusion compositions, both pre- and post- MIMiC correction, are provided in tables S5 and S6 of Supplementary Material S1. PEC correction requires the addition of 0.03 to 9.28 % olivine to restore melt inclusion compositions to equilibrium with their hosts. The average PEC correction is 3.85 % for São Jorge (SJ) MI and 2.17 % for the two recent eruptions. Following PEC correction, melt inclusion compositions range 39.87–45.74 wt% SiO_2, 4.00–7.36 wt% MgO, 3.02–5.20 wt% Na_2O, and 8.36–11.57 wt% FeO_t. On the total alkali-silica diagram (Fig. 4a), the PEC-corrected MI span the foidite to basanite compositional fields, with the most SiO_2-rich MI (41.74–45.74 wt%) overlapping the range of the whole-rocks (compositions given in Lo Forte et al., 2023) and of bulk rocks from the literature (Hildner et al., 2011, 2012; Mata et al., 2017). These MI have MgO contents varying from 4.00 to 5.76 wt%, TiO_2 from 2.44 to 3.06 wt%, and P_2O_5 from 0.84 to 1.36 wt%. The CaO/Al_2O_3 ratios vary between 0.88 and 0.97 for SJ MI, and between 0.44 and 0.84 for the 1951 and 2014/15 MI (Fig. 4b).

We model fractional crystallisation (FC) (Fig. 4b-d) to determine the extent of crystallisation at the time of entrapment, and to test if the melt follows the liquid line of descent (LLD) prior to be entrapped, or if instead points to some Fe-Mg diffusive exchange during crystallisation (Fig. 4b, c). We start our simulations with a hypothetic parental melt composition corresponding to the primitive lava Fogo 16 from Hildner et al. (2012) (MgO = 9.79 wt%; FeO = 12.03 wt%). We assume an initial H_2O content of 2.0 wt% (see below) and an oxygen fugacity of 1.5 log units above the Fayalite-Magnetite-Quartz buffer (ΔFMQ + 1.5; Moussallam et al., 2019). Starting from this parental melt composition and an initial temperature of 1150 °C, we simulate the cooling-crystallisation trajectory using Petrolog3 (Danyushevsky and Plechov, 2011), using the melt-mineral equilibrium models of Danyushevsky, (2001) for olivine, clinopyroxene, and plagioclase, and Ariskin and Barmina, (1999) for magnetite. Results (Fig. 4b,c,d) show that the modelled LLD accurately reproduces the whole-rock compositional trend. After PEC correction, MI also match more closely the LLD and the bulk rocks trend (Fig. 4b,c,d), implying diffusive Fe loss was minor (if any). No correction was therefore applied. All raw and corrected MI compositions are listed in Tables S5 and S6 of Supplementary Material S1.

4.4. Trace element composition

Table S5.2 of Supplementary Material S1 reports the concentrations of a selected suite of trace elements in the studied MI. The primitive mantle normalised trace element patterns (Fig. 5) (this study) match those of the bulk-rocks (Hildner et al., 2011, 2012; Mata et al., 2017). No negative Hf anomaly is observed, and the Zr/Hf ratios (averaging at 39)

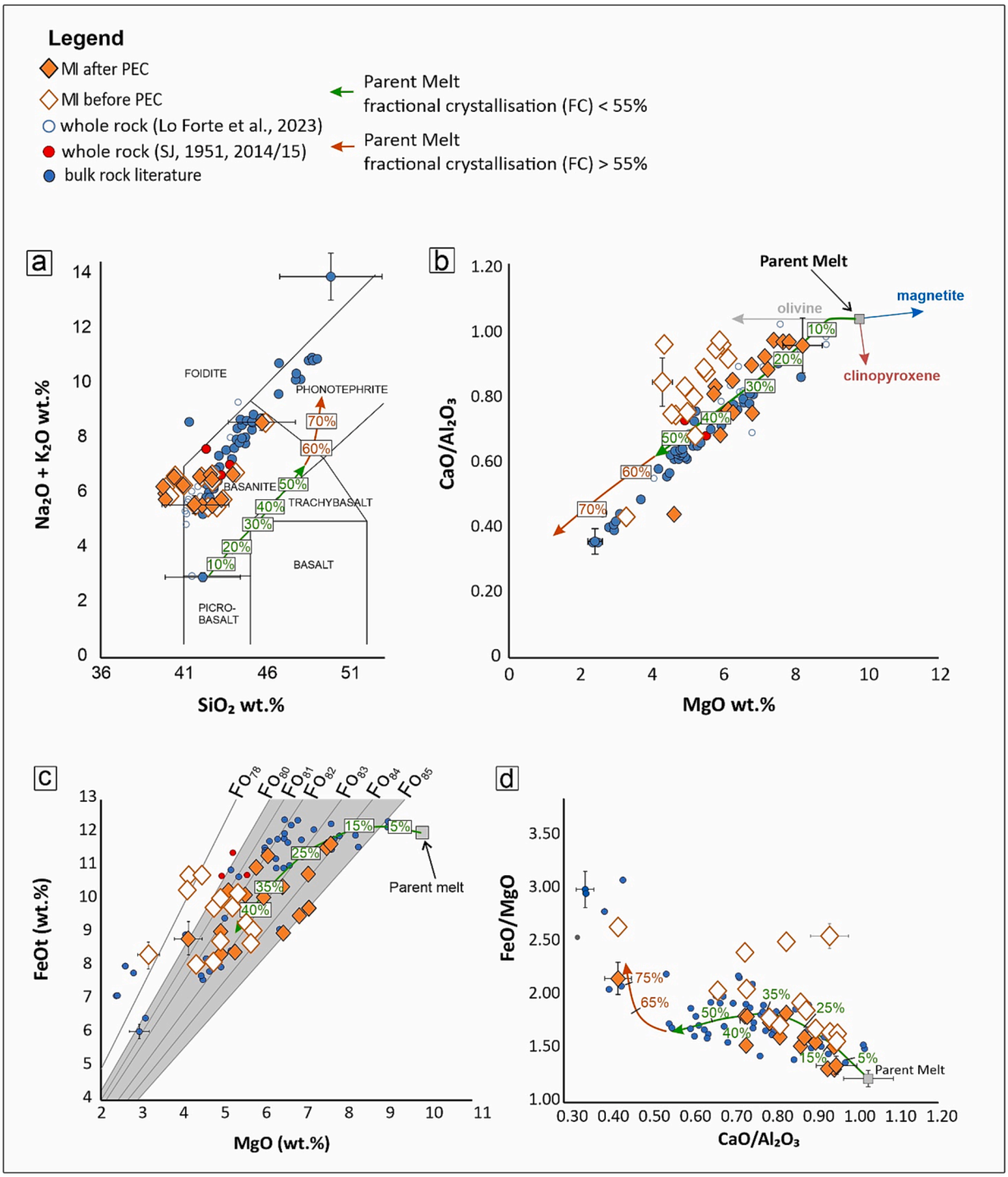

Fig. 4. Total alkali-silica diagram (a) and major element compositions of melt inclusions (b, c, d) together with whole-rock compositions from Hildner et al., (2011, 2012), Lo Forte et al. (2023) and Mata et al. (2017). The solid lines are liquid lines of descent (LLD), calculated from a primitive parent melt (SiO_2 42.14 wt%, MgO 9.79 wt%, FeO 12.03 wt%, Al_2O_3 12.41 wt%, CaO 12.96 wt%) using Petrolog3 (Danyushevsky and Plechov, 2011). The LLD are calculated assuming initial H_2O content of 2 wt% and oxygen fugacity of ΔFMQ + 1.5 (Moussallam et al., 2019). We used the melt-mineral equilibrium models of Danyushevsky (2001) for olivine, clinopyroxene and plagioclase, and of Ariskin and Barmina (1999) for magnetite. The orange LLD was calculated for FC > 55 %, to fit the more evolved MI (d). The grey area represents the range of forsterite component (Fo_{80-85}) in the analysed olivines hosting MI (a).

are comparable to the typical primitive mantle value (~36; Palme and O'Neil, 2003). The LILE (Large Ion Lithophile Elements)-enriched composition of Fogo melts is additionally corroborated by elevated Ba/La (15.0–20.3), Rb/Sr (0.05–0.07) and Rb/La (0.98–1.54) ratios (Weaver, 1991).

4.5. Volatiles

All the melt inclusion glasses are volatile-rich and contain 1.97 to 2.79 wt% H_2O and 9002 to 16044 ppm CO_2 in SJ MI (Fig. 6a). MI glasses from recent (1951–2014/15) eruptions are slightly less CO_2-rich than the SJ MI glasses and contain 1.20 to 2.92 wt% H_2O and 1239 to 9102 ppm CO_2 (Fig. 6; Table S5.1 Supplementary Material S1). CO_2 in MI

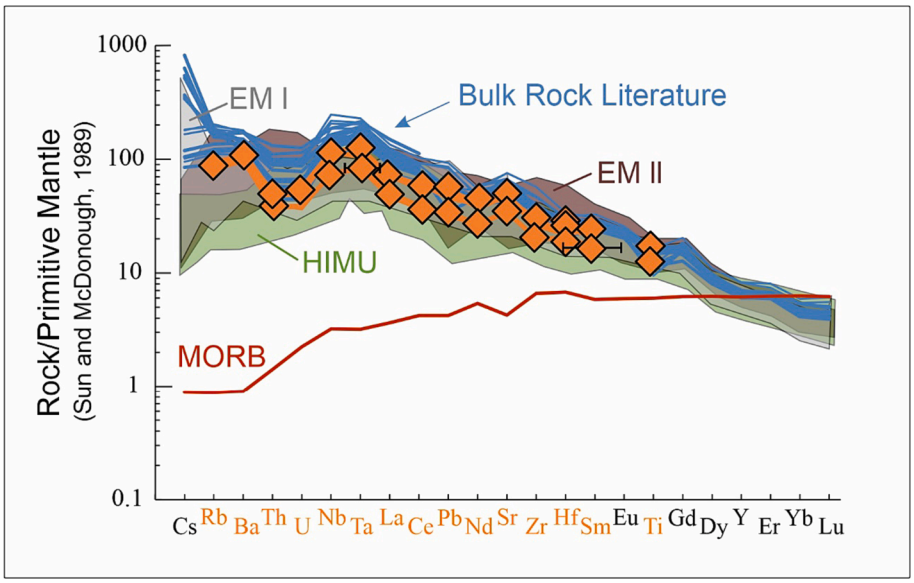

Fig. 5. Primitive mantle-normalised (Sun and McDonough, 1989) trace element patters in MI samples (orange patterns; average values from all samples are used). The trace element patterns are intermediate between the compositional ranges of enriched mantle sources (EM-I and EM-II; data from Willbold and Stracke, 2006) and the HIMU mantle source (Willbold and Stracke, 2006). Note the significant Nb and Ta enrichment relative to the light REE. The red line identifies the compositions of Mid-Oceanic Ridge Basalts (MORB; Sun and McDonough, 1989).

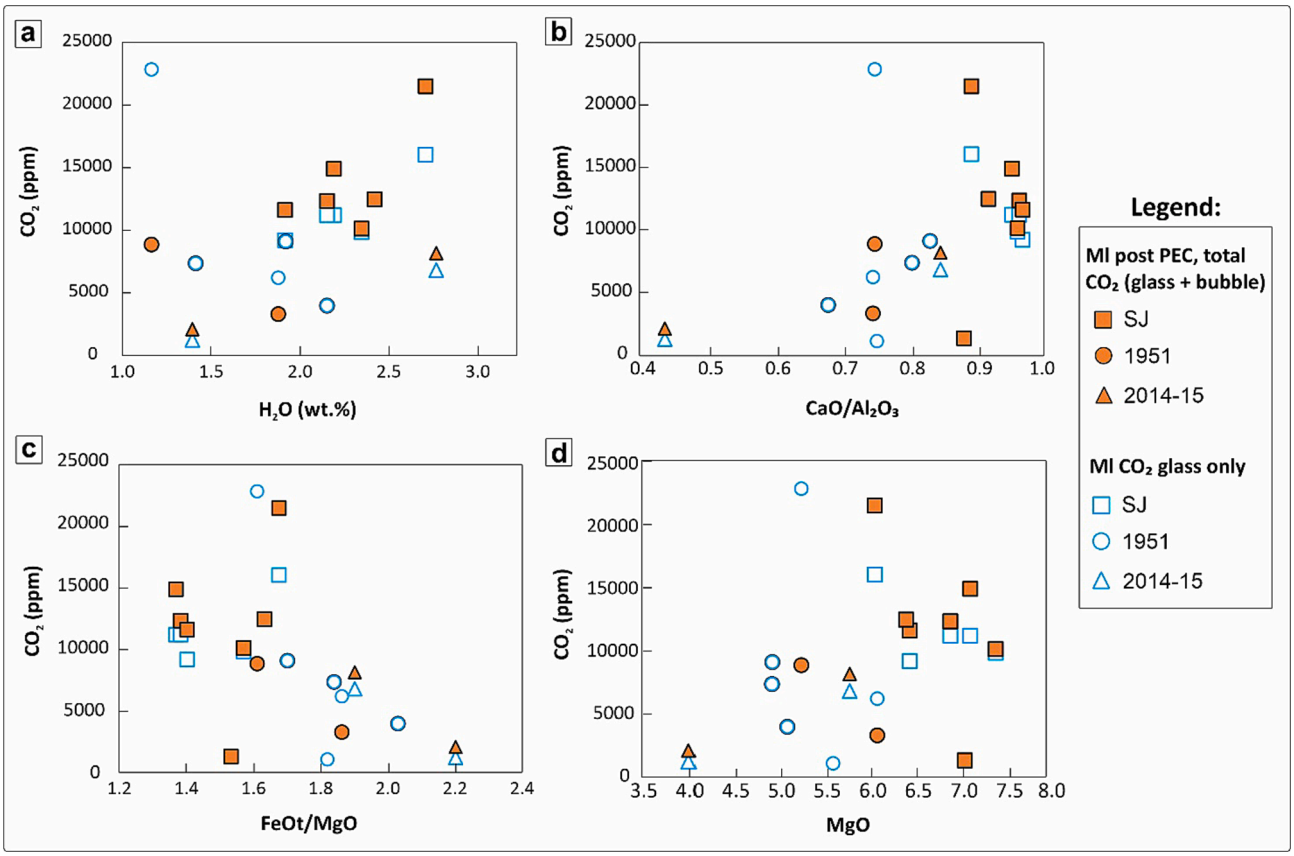

Fig. 6. CO_2 concentrations vs·H_2O (**a**), CaO/Al_2O_3 (**b**) and FeOt/MgO (**c**) ratios, and MgO (**d**). The SJ MI exhibit higher H_2O and CO_2 contents than those from the more recent eruptions in 1951 and 2014–15. The orange symbols represent data related to the total CO_2 content in the MI (glass + bubble), corresponding to measurements obtained through Raman-based total CO_2 estimates (see section 5.1 for further details).

glasses broadly decreases with increasing degree of melt evolution, e.g., with decreasing CaO/Al_2O_3 (Fig. 6b) and MgO (Fig. 6d) and increasing FeOt/MgO (Fig. 6c). The SJ MI glasses exhibit higher S concentrations (2676–7794 ppm) than the 1951 and 2014/15 MI (1146 to 5509 ppm) (values measured by nano-SIMS, Tables 5 and S5.1 Supplementary Material 1). Chlorine concentrations, measured by nano-SIMS, range

from 947 to 1358 ppm in SJ MI and from 956 to 1415 ppm for the recent eruptions. The measured fluorine concentrations are 1285–2216 ppm in SJ MI glasses and 1617–2249 ppm in the 1951–2014/15 MI glasses. For each element, a general least-squares linear regression was calculated, along with both 95 % confidence and prediction intervals. This process allowed us to extract an error associated with the estimation through the 95 % confidence interval for each measurement corrected by the determined linear regression. Subsequently, this error was quadratically added to the measurement itself. The absolute and relative errors were most pronounced for very low concentrations outside the range covered by our set of standards. As we extrapolated to higher concentrations, absolute errors increased. However, for measured concentrations (on average, >2000 ppm), the relative error rose less drastically compared to lower concentrations. For further details, please refer to Table S9 in Supplementary Material S1 and Figure S2 in Supplementary Material S2. The PEC-corrected concentrations vary as follows: 1.9–2.7 wt% (SJ MI) and 1.2–2.8 wt% (1951 and 2014/15 eruptions) for H_2O (Fig. 6a); 2621–7718 ppm (SJ) and 1120–5250 ppm (1951–2014/15) for S; 917–1328 ppm (SJ) and 934–1415 ppm (1951–2014/15) for Cl (Fig. 7). As typical of alkaline magmas in general (Webster et al., 2018), the Fogo MI glasses are especially Cl- and F-enriched (up to 1415 and to 2249 ppm) relative to other OIB localities (Fig. 7), being only matched by the El Hierro basanite MI (Taracsák et al., 2019). The Fogo MI have F/Cl ratios in the 1.2 to 2.4 range, i.e., higher than F/Cl values of most arc magmas, exception made for F/Cl reaching 2.5 in the Trans Mexican arc (Vigouroux et al., 2008) and in the Central American arc (Sadofsky et al., 2008; Fig. 7). This F-rich signature is a distinctive characteristic of OIB magmas in general (Kendrick et al., 2014).

5. Discussion

5.1. Reconstructing the total (glass + bubble) CO_2 content in MI

Our results show that the Fogo MI glasses contain up to ~1.6 wt% CO_2 (Fig. 6), plus ~2 wt% H_2O and ~0.48 wt% S, on average. However, all MI also contain CO_2-rich bubbles (Fig. 2). There is a positive relationship between total MI volumes and bubbles volumes (Fig. 8a), indicating that all MI contain similarly low bubble volumetric fractions (0.2–8.6 %). We conclude that the contemporaneous entrapment of melt and fluid inclusions is unlikely (Rasmussen et al., 2020), and therefore

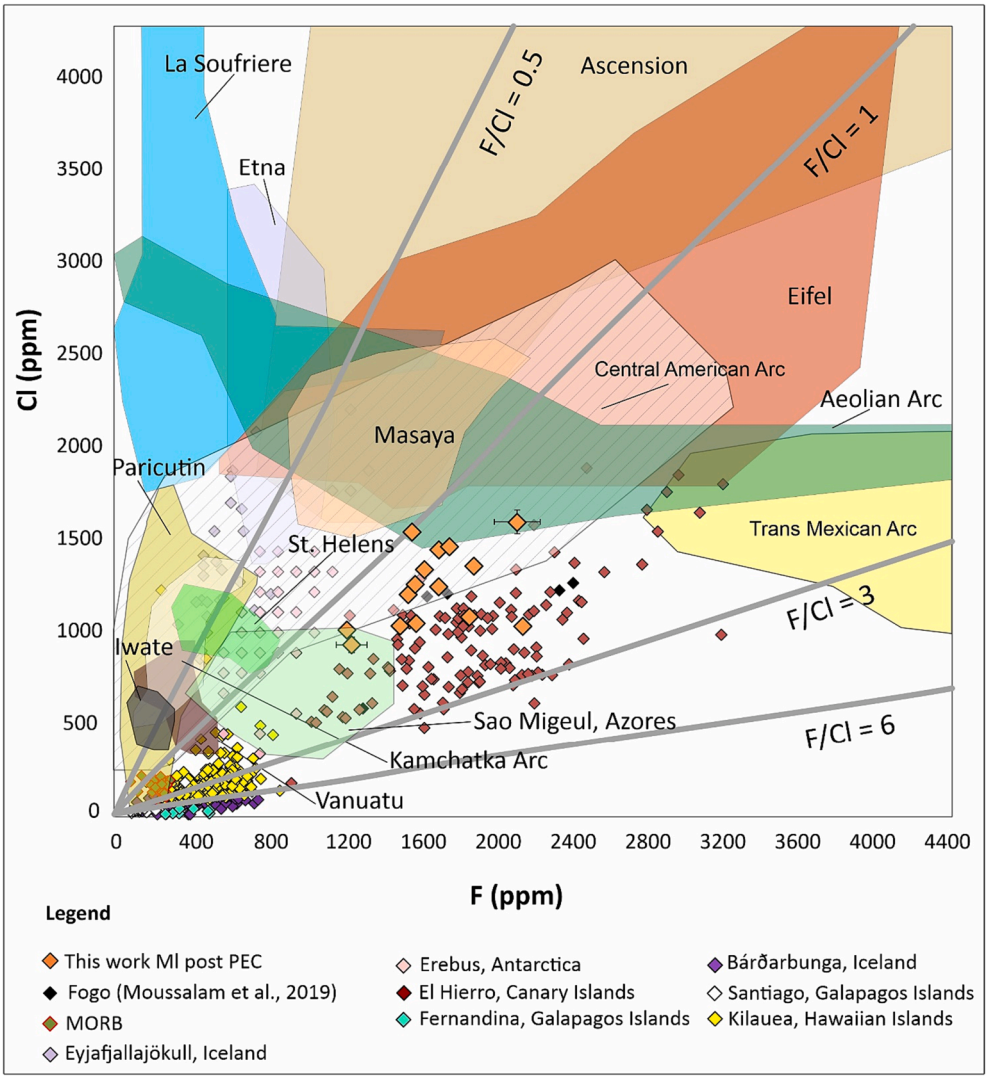

Fig. 7. In the F vs. Cl plot, our data are compared to MI of different OIB localities and from volcanoes of different geodynamic contexts, such as Ascension (Webster and Rebbert, 2001), Etna (Métrich et al., 1993, 2004), La Soufriere (Heath et al., 1998), St. Helens (Blundy and Cashman, 2005), Parìcutín (Rowe et al., 2011), Trans Mexican belt (Vigouroux et al., 2008), Central American belt (Sadofsky et al., 2008), Vanuatu (Métrich et al., 2011), Eifel (Harms and Schmincke, 2000), Aeolian islands (Di Martino et al., 2011), Masaya (Pérez et al., 2020), and Kamchatka volcanoes (Portnyagin et al., 2011). The F/Cl ratios of our MI (1.16–2.41) fall in the field of OIB volcanoes and partially overlap the composition of El Hierro MI.

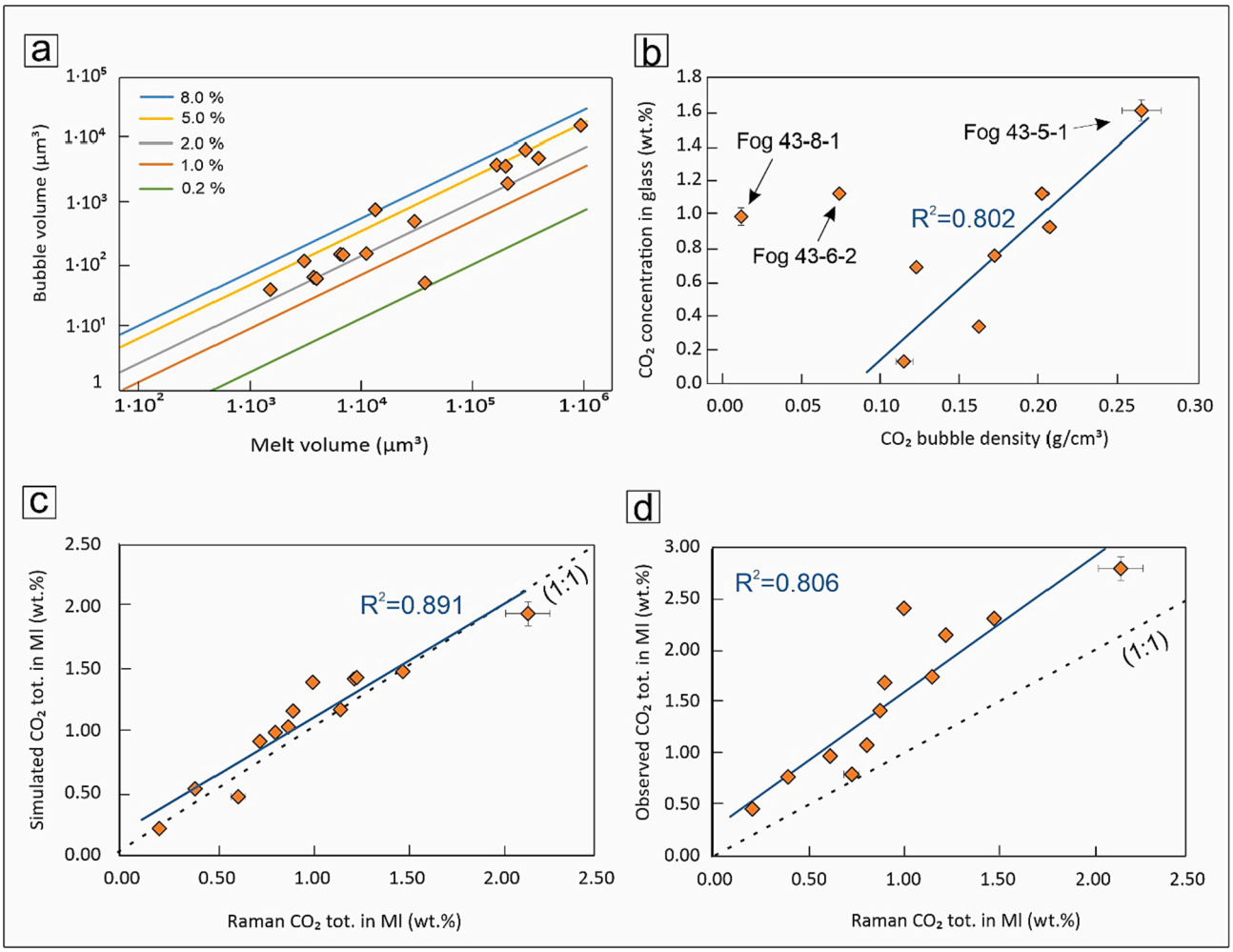

Fig. 8. **(a)** Plot of bubble volumes as a function of MI volumes; isovolumetric lines corresponding to bubble/MI volume ratios of 0.2 %, 1.0 %, 2.0 %, 5.0 %, and 8.0 % are also shown. **(b)** The plot shows a positive correlation between the CO_2 calculated in the glass and the density of the shrinkage bubble, except for the two samples (Fog 43–8-1 and 43–6-2) which exhibit intense Raman peaks associated with carbonates, specifically Fe-magnesite and nahcolite crystals on the bubble wall (Fig. 2). As shown in (b), the overlooked presence of carbonates in the bubble leads to an underestimation of the total CO_2 content. Excluding these two outliers, the samples show a good correlation ($R^2 = 0.802$). Plot of the total CO_2 concentration in MI, calculated using the Raman and Simulated methods **(c)** and the Raman and Observed methods **(d)**. In plot **(c)**, there is a strong correlation ($R^2 = 0.891$), with CO_2 concentrations from Raman and Simulated-volume methods showing a 1:1.1 relationship. In contrast, in plot **(d)**, the total CO_2 calculated using the Raman and Observed-volume methods is not strongly correlated ($R^2 = 0.806$), with a ratio of 1:1.6. The dashed lines correspond to a ratio 1:1.

all fluid bubbles found are shrinkage bubbles. Hence, as recently demonstrated elsewhere (Taracsák et al., 2019), reconstructing the total MI CO_2 budget requires a procedure in which the CO_2 masses contained in (i) shrinkage bubbles and (ii) glass are both fully taken into account.

The CO_2 mass contained in the glass is initially calculated by multiplying glass mass in the MI (glass density × glass volume) by CO_2 concentration in the glass (cfr. 4.5). Glass density is derived using MIMiC (Rasmussen et al., 2020), which uses the relationships of Lesher and Spera (2015), while glass volume is estimated following the procedure of Moore et al. (2015).

Next, we quantify shrinkage bubble CO_2 using three different, independent methodologies: (i) the Raman method (Esposito et al., 2011; Hartley et al., 2014; Moore et al., 2015; Rasmussen et al., 2018); (ii) the Simulated-volume method (Rasmussen et al., 2020); and (iii) the Observed-volume method (e.g., Shaw et al., 2010; Wanless et al., 2014; Hauri et al., 2018; Tucker et al., 2019). Our aim is to use the level of agreement/disagreement of these different methods as a proxy for the level of accuracy/inaccuracy of such bubble CO_2 estimates (Fig. 8).

In the Raman method (Hartley et al., 2014; Moore et al., 2015; Moore and Bodnar, 2019; Rasmussen et al., 2020), the bubble CO_2 mass is derived as the product of bubble CO_2 density × bubble volume. Raman indicates a pure-CO_2 gas phase composition for the shrinkage bubble (Fig. 2 a); we hence apply the densimeter by Wang et al. (2011) for the calculation of the bubble CO_2 density.

The other two CO_2 estimates (Simulated and Observed) are derived using the MiMiC code (Rasmussen et al., 2020). The Simulated-volume method relies on estimating bubble volumes and CO_2 contents from modelling the growth of bubbles during the cooling and quenching of the melt inclusions (rather than directly measuring bubble volumes). This bubble growth model assumes that exchange of CO_2 between melt and bubble terminates at a CO_2 closure temperature (T_c) for diffusion (generally higher than the glass-transition temperature) followed by further bubble expansion with no CO_2 loss to bubble (Rasmussen et al., 2020).

Finally, the Observed-volume method (e.g., Shaw et al., 2010; Wanless et al., 2014; Hauri et al., 2018; Tucker et al., 2019) uses directly measured bubble volumes and entails determining the CO_2 mass within the vapor bubble by applying the modified Redlich-Kwong (MRK) equation of state. The method relies on the assumption that vapor-melt equilibrium is maintained throughout the entire bubble quenching/growth history. The temperature of vapor-melt equilibrium is determined based on the calculated glass-transition temperature, which

however can vary significantly by several hundred degrees Celsius, depending on factors such as melt viscosity and cooling rate (Giordano et al., 2005).

All three CO_2 restoration methods have their caveats and limitations which can potentially lead to overestimation/underestimation of the total MI CO_2. Use of the Raman restoration method (e.g., Esposito et al., 2011; Moore et al., 2015), in particular, is challenged by difficulties in (i) correctly measuring melt inclusion geometry, and hence glass vs. bubble volumes (Moore et al., 2015) and (ii) quantifying the relative volumetric fractions occupied by minerals and fluid in the bubble (Schiavi et al., 2020). Determination of melt inclusion geometry (glass and bubble volumes) in principle requires accurate 3D scanning microtomographic analysis, which is rarely available. Our glass/bubble volumes (Table S7 of Supplementary Material S1) are estimated from 2D analysis, and on the assumption that the length of the third semi-axis c (normal to the polished plane) equals to the arithmetic mean of axes a and b (Moore et al., 2015); this assumption should, at least in principle, introduce a relatively minor (5 %) error (Wallace et al., 2015). More problematic is to account for the carbon mass sequestered in mineral phases inside the bubble. Recent studies have found that mineral phases such as carbonates, sulphides, sulphates and native sulphur can precipitate inside bubbles during cooling (e.g., Kamenetsky et al., 2002; Hartley et al., 2014; Moore et al., 2015; Esposito et al., 2016; Robidoux et al., 2018; Guzmics et al., 2019; Tucker et al., 2019; Schiavi et al., 2020; Venugopal et al., 2020; Buso et al., 2022; Feignon et al., 2022). Precipitation of these minerals can potentially sequester large fractions of the bubble-carried CO_2, hence ignoring their presence can result in significant (up to 40 %) underestimation of the total MI CO_2 (Schiavi et al., 2020). We detected the presence of carbonate phases, such as Fe-magnesite and nahcolite (Supplementary Material S2 Figure S2), and sulphates, in roughly 50 % of the Raman spectra. The proportions of the different phases are highly variable. Raman microtomography revealed significant volumes of carbonates crystallised on the walls of the MI Fog 43–6-2 bubble, amounting to ~35 vol% according to an approximate average estimate based on few 2D sections extracted from the 3D map (Supplementary Material S2 Figure S2). This corresponds to ~25 % of the CO_2 sequestered in the bubble (compared with 9 % reported in Table S7 of the Supplementary Material S1). We conclude that the total CO_2 content can be underestimated (by about 15–20 % for MI Fog 43–6-2) if carbon stored in carbonates inside the bubble is neglected. However, considering the overall positive correlation observed between glass MI CO_2 and shrinkage bubble density (Fig. 8b), we conclude that precipitation of carbonates is likely to be marginal in all samples except Fog 43–8-1 and 43–6-2 (that coherently exhibit the most intense Raman peaks associated with carbonates).

The second CO_2 restoration methodology used (Simulated-volume method) overcomes some of the limitations above, as it does not rely on measured bubble volumes, but rather on estimated bubble volumes based on modelling bubble growth during MI cooling and quenching. The detailed sensitivity study of Rasmussen et al. (2020) demonstrates that the amount of cooling experienced by MI, from their entrapment temperature (T_e) to their CO_2 closure temperature (T_c), is the key parameter controlling the extent of CO_2 loss to bubbles. According to Rasmussen et al. (2020), this cooling extent ($T_e - T_c$) depends on MI dimension (measured texturally) and cooling rate, for which we unfortunately have no independent estimate. In such conditions, MIMiC adopts a calculated cooling rate derived by solving the Dodson equation for the magnesium closure temperature (T_c(MgO)); this procedure can potentially introduce a maximum error of 50 % on the restored CO_2 concentrations (when the used T_c(MgO) is in excess of by one order of magnitude).

Finally, the Observed-volume method calculates the CO_2 mass in the bubble by applying an equation of state and performing a mass balance. In this approach, the observed bubble volume, measured under the microscope, used in the calculation assumes that melt-bubble equilibrium is maintained throughout the entire bubble growth history. However, if equilibrium is not maintained, the calculation based on the observed volume may not be accurate. Additionally, this method assumes the glass transition temperature (T_g) as the final melt-bubble equilibrium temperature, but precisely assessing T_g is complicated by its strong dependence on factors such as cooling rate, melt composition, melt viscosity, and volatile content (Rasmussen et al., 2020).

Ultimately, since all restoration methods have limits and caveats, a multi-method approach is advisable (Rasmussen et al., 2020). The outputs of the three restoration methods used here are compared in Fig. 8c and 8d. We find that the Raman spectroscopy measurements and simulated-volume approach yield CO_2 concentrations that agree within 9.7 % on average (range: 0.4–22.6 %). The agreement between these two independent methodologies provides confidence in our restored total MI CO_2 values. The total MI CO_2 contents determined with the observed-volume method also positively correlate with those inferred from Raman analysis (Fig. 8d), but typically plot above the 1:1 line, indicating that the observed-volume approach may systematically overestimate the MI CO_2 budget, as already suggested (Moore et al., 2018; Rasmussen et al., 2020). Rasmussen et al. (2020) also found that the concentrations reconstructed from both Raman measurements and the simulated-volume method are quantitatively consistent with those obtained by re-homogenising MI at high temperature and pressure – this latter procedure being considered as that yielding the most accurate CO_2 reconstructions. Ultimately, while we are well aware of the many existing potential sources of uncertainty, we conclude that our calculations bring nonetheless robust evidences that (i) in some cases of OIB MI, a large fraction (up to 50 %) of the MI CO_2 is contained in the bubbles (Mironov et al., 2015), and (ii) the total (glass + bubble) CO_2 content in the Fogo parental melt is certainly > 1 wt%, and potentially as high as ~2 wt% (the highest value obtained by the Raman and Observed-volume methods). For the sake of simplicity, in the discussion below we refer to the Raman-based bubble (and hence total) CO_2 estimates, but we note that these overlap with those derived from the bubble growth model using MiMIC by a factor of < 10 %.

5.2. A CO_2-rich parental melt

Finally, glass CO_2 mass and shrinkage bubble CO_2 mass are summed to obtain total CO_2 mass in MI, which is ultimately converted in total CO_2 concentration in the MI. All calculations, for each MI analysed, are

Table 1
Summary of the total CO_2 content (bubble + glass) calculated in the analysed melt inclusions using three different methods (Raman, Simulated, and Observed).

Sample	CO_2 wt% in MI (Raman Method)	CO_2 wt% in MI (Simulated Method)	CO_2 wt% in MI (Observed Method)
Fog 43-3-1	1.25	1.43	/
43-5-1	2.15	1.95	2.75
43-6-1	1.49	1.48	2.31
43-6-2	1.23	1.42	2.15
43-6-3	1.16	1.18	1.74
43-6-4	/	/	/
43-7-1	0.13	/	/
43-8-1	1.01	1.40	/
Fog 8-1-1	0.40	0.54	0.77
8-4-1	0.89	1.03	1.41
8-7-1	0.74	0.92	0.79
8-8-1	0.91	1.16	1.69
8-11-2	0.62	0.47	0.97
8-11-3	/	/	/
8-11-4	0.11	/	/
8-11-5	/	/	/
Fog 11-2-1	0.21	0.22	0.46
11-3-1	0.82	0.99	1.08

given in Table 1 and in Table S7 of Supplementary Material S1. Using the Raman method results described above, we find that bubbles contain 281–5546 ppm CO_2 (for the SJ MI) and 857–2920 ppm CO_2 (for the 1951 and 2014/15 MI). The total CO_2 contents thus range from 1309 to 21502 ppm for SJ MI, and from 1084 to 9102 ppm for the 1951 and 2014/15 eruptions (Fig. 6). We thus estimate that 3 to 47 % of the total MI CO_2 content is contained in the bubbles.

Our results show that the basanitic melts from Fogo are exceptionally CO_2-rich. Their volatile-rich nature is additionally demonstrated by high halogen contents (Fig. 7). The estimated CO_2 content of the parental melt (2.15 wt%) is up to a factor 10 higher than for other OIB localities (e.g., Erebus in Antarctica, Moussallam et al., 2014; Fernandina and Santiago in the Galapagos, Koleszar et al., 2009; Piton de la Fournaise in Reunion Island, Di Muro et al., 2014; Kilauea in the Hawaii, Sides et al., 2014; Wieser et al., 2021; Pico in the Azores, Métrich et al., 2014) and Iceland (e.g., Bardabunga, Bali et al., 2018, and Laki, Hartley, 2014) (Fig. 9a). In addition to confirming that bubbles do matter if the CO_2 MI budget is to be reconstructed (Moore et al., 2015; Rasmussen et al., 2020; Buso et al., 2022), our results also corroborate recent work that shows that alkali rich OIB magmas can be especially carbon-rich, as observed at El Hierro (CO_2 up to 4 wt%; Longpré et al., 2017; Moussallam et al., 2019; Taracsák et al., 2019) and La Palma (3–5 wt%; e.g., Burton et al., 2023) in the Canary Archipelago, and at Piton de La Fournaise in La Reunion Island (3.5 ± 1.4 wt%, Boudoire et al., 2018) (Fig. 9a) Our results are consistent with those recently reported by DeVitre et al. (2023), who obtained similarly high volatile contents in primitive MI (melt Mg#70–71%) from Fogo: ~2.0 wt.% CO_2, 2.8 wt.% H_2O, 0.6 wt.% S, 0.11 wt.% Cl, and 0.19 wt.% F. (note that in these studies shrinkage bubble CO_2 has been accounted for with either observations or modelling). The fact that alkali rich OIB volcanoes erupted magmas richer in CO_2 than alkali poor OIBs has been documented at a global scale (Sun and Dasgupta, 2023), although we see no evidence in our MI of the extremely high (9–10 wt%) CO_2 contents inferred by these authors for the Cape Verde archipelago parental melts. Rather, the ~2 wt% CO_2 content we estimate for the Fogo parental melt is at the lower range of the measured/inferred (Hudgins et al., 2015; Aiuppa et al., 2021) CO_2-enriched signatures of alkaline mafic melts from continental rift context (e.g., in the East African rift system; Foley et al., 2012). This link between high CO_2 compositions and melt enrichment in alkalis (and other incompatible elements; Aiuppa et al., 2021) is further explored below (Fig. 10).

5.3. Clues from CO_2 vs. trace-element correlations

A potentially useful approach to test the accuracy of our reconstructed MI CO_2 content is to normalize them to the measured Nb and Ba contents in the same MI glasses (Fig. 10). These trace elements are thought to have similar bulk mineral/melt distribution coefficients to that of carbon (e.g., Rosenthal et al., 2015; Hirschmann, 2018). Hence, the CO_2/Nb and CO_2/Ba ratios should not be fractionated during mantle

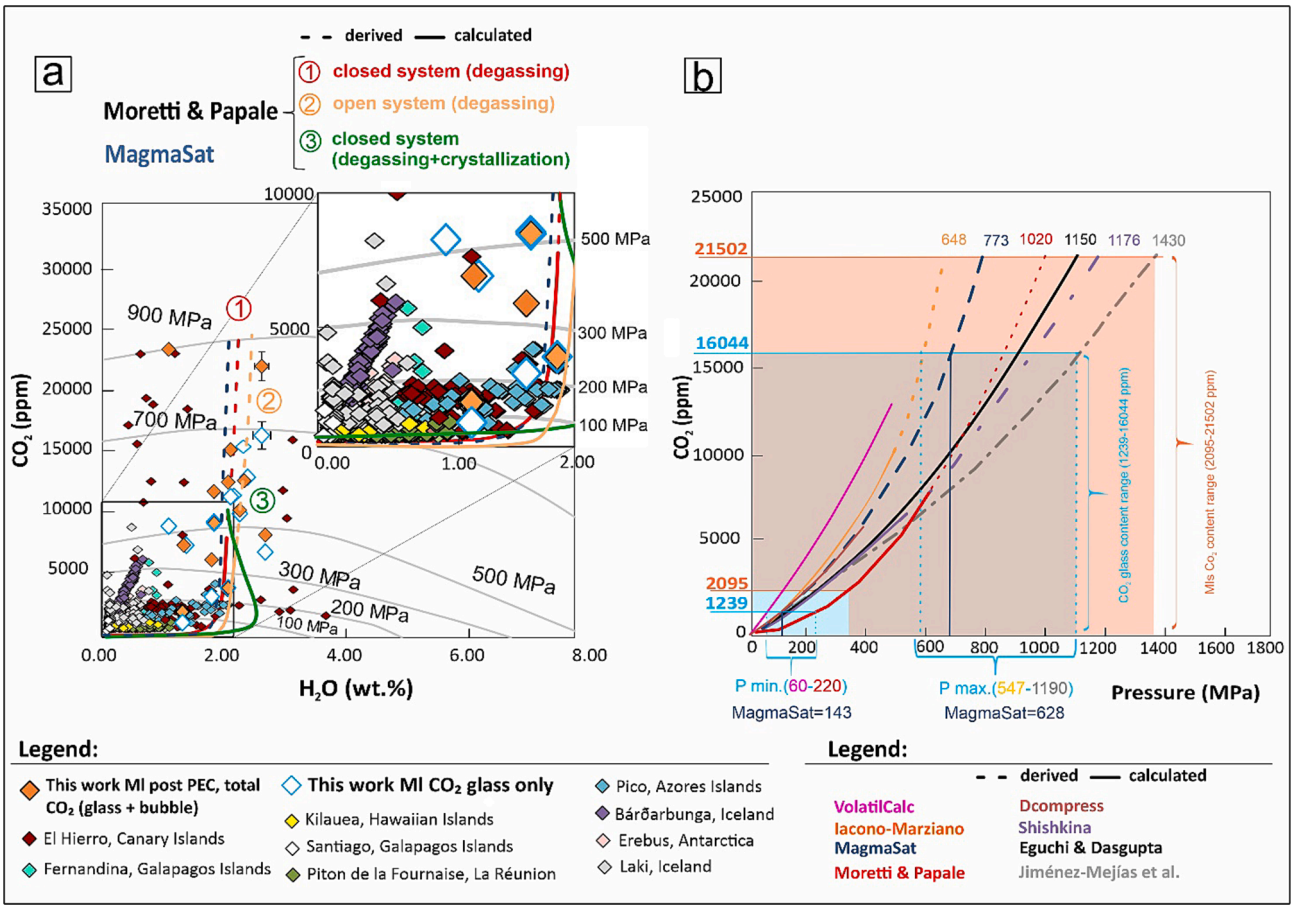

Fig. 9. (a) H_2O and CO_2 concentration in studied MI and in other OIB occurrences. Isobars were calculated using an average composition of our MI samples at temperature of 1150 °C and an oxygen fugacity of ΔFMQ + 1.5 (Moussallam et al., 2019). Degassing paths, in a closed system, were calculated using the volatile saturation models by Moretti et al. (2003) and MagmaSat (Ghiorso and Gualda, 2015), incorporated into VESIcal web portal (Iacovino et al., 2021), with the same input melt composition and temperature and volatile contents of 21502 ppm and 2.0 wt% for CO_2 and H_2O respectively. (b) In the CO_2 content vs. Pressure graph, different saturation models are compared. The solid lines represent the outputs of the different models, instead the dashed lines represent the extrapolations of these models.

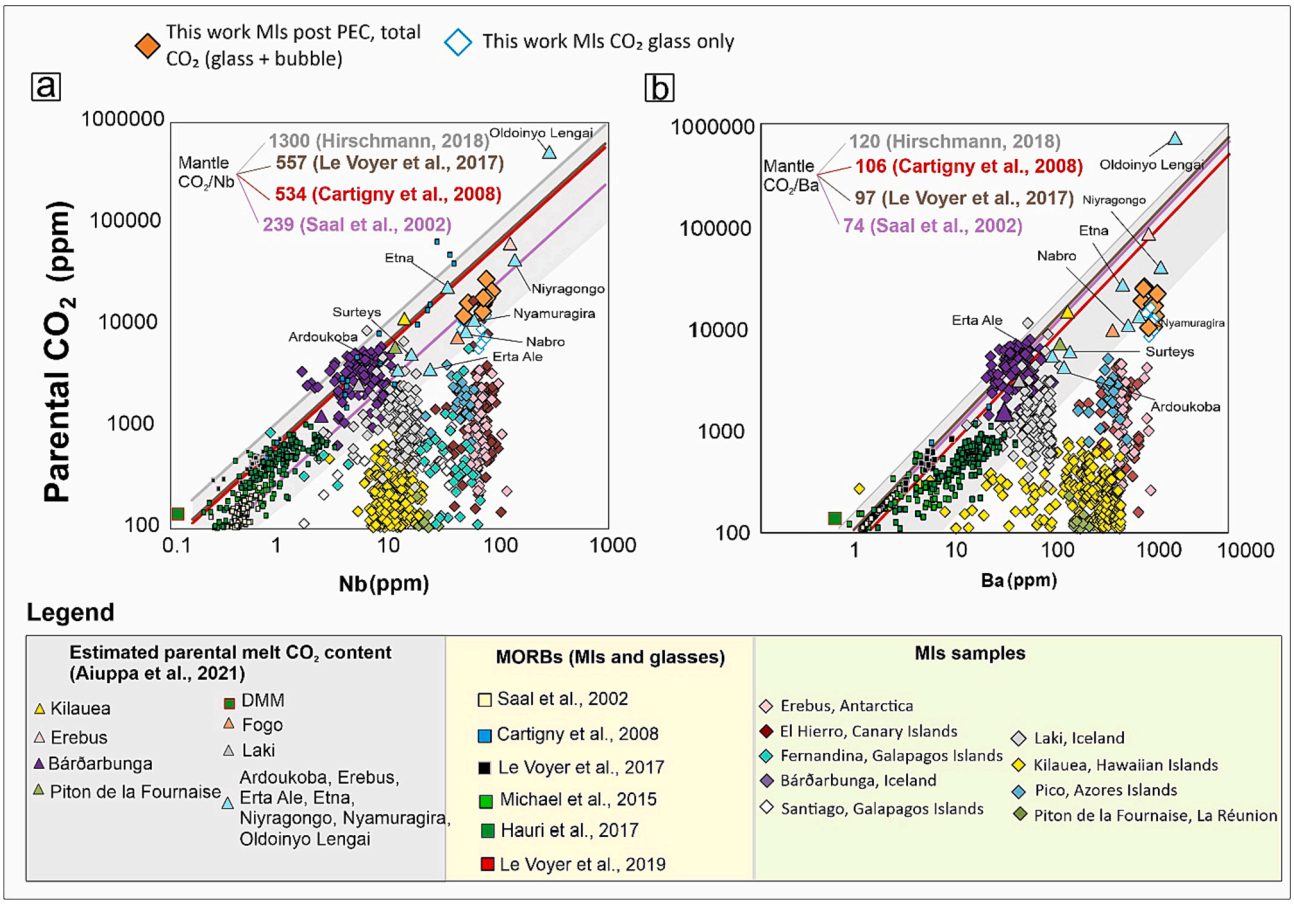

Fig. 10. CO_2/trace element ratios. (a) In the Nb versus CO_2 plot, most of the literature "degassed" MI and our MI with the CO_2 content measured in the glass only (white diamond with light blue border) plot below the CO_2-Nb mantle array (represented by the grey area), as defined by the un-degassed MI and glasses of the MORB (characteristic upper mantle CO_2/Nb ratios from refs. Saal et al., 2002; Cartigny et al., 2008; Le Voyer et al., 2017; Hirschmann, 2018). Contrarily, our MI with the total CO_2 content (orange symbol, CO_2 glass + CO_2 bubble) fall in the mantle array field. (b) same as (a) but using Ba. Our MI with the total CO_2 content fall within the CO_2/Ba mantle range, 74–120 (Saal et al., 2002; Cartigny et al., 2008; Le Voyer et al., 2017; Hirschmann, 2018). In contrast, literature "degassed" MI and our MI with CO_2 measured only in the glass plot below the CO_2/Ba mantle array.

melting and fractional crystallisation of mafic melts. If a mantle-sourced melt has not degassed CO_2 during crustal emplacement, it is thus expected to preserve a record of its source mantle CO_2/(Nb, Ba) ratio (e.g., Saal et al., 2002; Michael and Graham, 2015; Shimizu et al., 2016; Le Voyer et al., 2017; Hauri et al., 2018; Tucker et al., 2019). Following these premises, the expected range of mantle CO_2/Nb (Fig. 10a) and CO_2/Ba (Fig. 10b) have been inferred (see grey filled diagonal bands in Fig. 10) from analysis of MORB that, owing to their volatile-depleted nature, are thought not to have reached volatile saturation before eruption (undegassed MORB; Michael and Graham, 2015) or entrapped as MI (e.g., Saal et al., 2002; Le Voyer et al., 2017; Moussallam et al., 2023). OIB magmas, in contrast, owing to their volatile enriched nature, do systematically reach saturation during ascent (Dixon and Stolper, 1995) and, even more significantly, form post-entrapment shrinkage bubbles that can sequester a large fraction of the MI CO_2 upon cooling and decompression (Hartley et al., 2014; Moore et al., 2015; Wallace et al., 2015; Tucker et al., 2019; Schiavi et al., 2020). As noted above, most MI results from the literature refer to glass measurements only, in which no correction for CO_2 in the bubbles has been attempted (with exceptions; Taracsák et al., 2019; Tucker et al., 2019); unsurprisingly, these plot below the mantle field in Fig. 10, implying their CO_2/trace element ratios underestimate the source mantle ratios, owing to extensive CO_2 loss to bubbles, pre- and post-entrapment (e.g., Hartley et al., 2014).

Considering the highest reconstructed total CO_2 contents only, our MI exhibit a relatively narrow range of CO_2/Nb (277–283) and CO_2/Ba (26–22) (Fig. 10). This is at the lower limit (CO_2/Nb), or below (CO_2/Ba), the interval of representative ratios proposed for the upper mantle, based on the analysis of MORB MI and/or undegassed MORB glasses (Fig. 10). It is important to recall that, in their recent global compilation, Sun and Dasgupta (2023) have proposed that the mantle source of OIB volcanism is characterised by higher CO_2/Nb (~1850) and CO_2/Ba (~226) ratios than the depleted mantle source feeding MORB volcanism. Overall, Fig. 10 indicates that, in spite of our applied correction for CO_2 in shrinkage bubbles, our reconstructed total CO_2 concentrations likely still underestimate the real parental melt CO_2 contents, potentially because of early (before MI formation) CO_2 separation from melt into the vapour phase (e.g., Rosenthal et al., 2015; Le Voyer et al., 2017; Hirschmann, 2018; Aiuppa et al., 2021).

5.4. *High CO_2 implies deep magma storage*

The important implication of the high CO_2 contents of the studied MI is that magma must be stored deep in the Fogo plumbing system prior to eruption (Fig. 9b, 11). To demonstrate this, we use the inferred H_2O-CO_2 MI concentrations (Fig. 9a), in combination with available saturation models (Fig. 9b), to estimate the MI entrapment pressures (assuming MI are volatile saturated at the time of their entrapment). However, the conversion of volatile contents into pressures requires selection of one of the several saturation models existing in the literature (e.g., MagmaSat, Ghiorso and Gualda, 2015; Iacono-Marziano et al., 2012; D-Compress, Burgisser et al., 2015; Moretti et al., 2003; VolatileCalc, Newman and

Lowenstern, 2002; Jiménez-Mejías et al., 2021; Shishkina et al., 2014), all of which have been calibrated over different compositional ranges and at relatively low pressures, and hence for lower CO_2 concentrations than the concentrations considered here). In addition to being calibrated at relatively low pressures (<800 MPa, the model of Eguchi and Dasgupta, 2018 being the only exception), these different volatile saturation models predict CO_2 solubilities in Fogo melts that are highly variable, and typically span a factor 2 to 4 (or more) from the least and the most conservative estimate (Fig. 8b). This implies that, for a given MI CO_2 content, a range of MI entrapment pressures can be derived, with the VolatileCalc and Iacono-Marziano et al. (2012) models typically returning the lowest entrapment pressures, and the Jiménez-Mejías et al. (2021) model the highest (Fig. 9b). It is important to remind that some of these models have been calibrated for tholeiitic compositions, and their results are therefore shown for illustrative purposes only. The MagmaSat model outputs some intermediate entrapment pressure conditions in all cases (Fig. 9b).

We focus on the range (2095–21502 ppm) of total CO_2 contents, which converts into a minimum–maximum range of entrapment pressures of 100–290 MPa (217 MPa with MagmaSat) for the most CO_2-depleted inclusion (Fog 11–2-1; 0.21 wt%) and to 648–1430 MPa (773 MPa with MagmaSat) for the most CO_2-rich inclusion (Fog 43–5-1; 2.1 wt%). The upper range of MI entrapment pressures is higher than the pressures obtained previously at Fogo using clinopyroxene-liquid barometry (300–750 MPa) and fluid inclusion microthermometry (200–740 MPa) (Hildner et al., 2011, 2012; Klügel et al., 2020; Lo Forte et al., 2023). Ultimately, these pressures indicate MI may have been entrapped during early olivine crystallisation at depths of 26 to 35 km, well within the lithospheric mantle (extending from ~12 to ~60 km depth underneath Fogo Island; Liu et al., 2021).

We then use the composition (major elements and volatile contents) of this deeply trapped Fog 43–5-1 MI as the starting condition for model simulations of volatile degassing upon decompression. We run two model simulations of degassing using the saturation codes of Moretti et al. (2003) and MagmaSat (Ghiorso and Gualda, 2015). Both codes have been used previously to model magma degassing in a variety of volcanic systems erupting magmas of different composition (Aiuppa et al., 2007, 2010, 2017, 2022; Edmonds et al., 2010; Marini et al., 2011; Oppenheimer et al., 2011; Pino et al., 2011; Moretti 2013a, 2013b; de Moor et al., 2016; Bamber et al., 2022; Halldórsson et al., 2022; Romero et al., 2023; Sharpe et al., 2022; Boulanger and France, 2023; Liu et al., 2023; Mitchell et al., 2023). With both volatile saturation codes, we model dissolved volatile contents in melt along a closed-system decompression path, starting from 1200 MPa pressure (final pressure, 0.1 MPa), in isothermal conditions (T = 1150 °C), and at ΔFMQ + 1.5. Results of our model calculations, illustrated in Fig. 9a, indicate that the modelled melt volatile compositions reproduce well the range of H_2O-CO_2 contents measured in our MI (Fig. 9a), providing confidence in our choice of volatile saturation models and model output. For comparison, we also show in Fig. 9 the modelled degassing path calculated for (i) isothermal decompression in open-system conditions (orange curve) and (ii) non-isothermal (temperature range, 1128–985 °C) closed-system degassing with crystallisation taken into account (green curve). The latter model trend was obtained by linking together (a) MI saturation pressures (from H_2O-CO_2 contents) with (b) MI major element compositions, and hence (by matching against the modelled LLD; Fig. 4) melt temperature and extent of crystallisation. The open system run predicts some extreme CO_2 depletions at low pressure (that are not observed in the MI dataset; see inset in Fig. 9a); while the non-isothermal closed system + crystallisation model trend predicts some larger (>2 wt%) H_2O enrichments at low pressure that potentially explain the composition of some more evolved El Hierro MI.

Our results (Fig. 9) suggest magma storage conditions at Fogo to be significantly deeper than previously thought. Previous work, based on fluid inclusion microthermometry (Hildner et al., 2011, 2012; Klügel et al., 2020; Lo Forte et al., 2023) and on clinopyroxene-liquid geothermobarometry (Hildner et al., 2011, 2012; Klügel et al., 2020), have revealed the existence of a complex, vertically stacked magma storage system, with a main zone at 17–25 ± 5 km depth (Fig. 11) overlain, in the 9–12 ± 2 km depth range, by a sequence of levels of temporary magma stagnation, where differentiation eventually takes place prior/during eruption (generating phono-tephritic melts, such as those erupted during the 1951, 1995 and 2014–2015 eruptions). Our volatile data, especially those of the CO_2-richest – and hence more deeply trapped – MI (2.15 wt%, Fog 43–5-1), extend the range of magma storage conditions downward. The entrapment (saturation) pressure range, inferred for this MI, is between 648 and 1430 MPa (i.e. about 20 to 45 km depth), depending on the saturation model used (see Fig. 9b). If we concentrate on the models that account for the increase of CO_2 solubility with melt alkalinity (and silica undersaturation), the inferred MI entrapment pressures are 773 (MagmaSat) and 1020 MPa (Moretti et al., 2003), respectively. With the mantle-crust reference model previously utilised by Lo Forte et al. (2023), these pressures correspond to entrapment depths of ~27 km (MagmaSat) and ~36 km (Moretti et al., 2003). The shrinkage bubble in this MI contains a small amount of minerals (cfr. 5.1), implying its Raman-derived CO_2 bubble density (and hence bubble CO_2 content) is not severely affected by mineral precipitation. Although it is well possible that the measured CO_2 content underestimates the real CO_2 content of the parental melt, because of pre-entrapment CO_2 loss to bubbles (cfr. 5.2), we interpret such MI saturation pressures as indicative of a deep magma storage at 31.5 ± 4.3 km depth, at (or nearby) a main geological boundary bounded by the Elastic effective Thickness (Te; located at ~30 km depth; Pim et al., 2008).

Ultimately, our data prove that pre-eruptive magma storage/ascent underneath Fogo occurs/starts within/from a deep magma storage zone at 31.5 ± 4.3 km, in the lithospheric mantle. This is right above a cluster of deep earthquakes (38–43 km depth; Leva et al. 2019) that may correspond to fracturing events during magma accumulation zone replenishment events with more deeply sourced melts, rising from the convecting mantle source (at > 60 km). Such deep pre-eruptive magma storage conditions are similar to those of other intraplate oceanic islands, e.g., El Hierro (Taracsák et al., 2019), Piton de la Fournaise (Boudoire et al., 2018), La Palma (Dayton et al., 2023), and the Azores islands (e.g., Zanon et al., 2023).

5.5. *High carbon in the source mantle, and implications for the global carbon cycle*

We use our parental melt CO_2 content inferred above (2.15 wt%) to estimate the carbon content in the mantle source feeding volcanism at Fogo. To this aim, we use a modal batch-melting equation (Shaw, 1970):

$$C_{pm} = \frac{C_0}{[F + D(1-F)]} \cong C_0/F \quad (1)$$

in which C_{pm} stands for the CO_2 in mantle-derived parental melts (2.15 wt% in our case), C_0 is the initial abundance of CO_2 in the source mantle, D is the CO_2 solid-melt partition coefficient (assumed at 0.00055; Rosenthal et al., 2015), and F is the melt fraction (0 to 1). This partial melting degree F in the Fogo mantle source is estimated at 0.06–0.07 by using MI major element composition to derive the final stage mantle-melt equilibration temperature (~1597 °C) and pressure (~4.8 GPa), and hence melting degree, according to the methodology of Sun and Dasgupta (2020, 2023). With these numbers, the 2.15 wt% parental melt CO_2 content converts into 355–414 ppm C in the Fogo mantle source.

We caution our estimated carbon range should be considered as a conservative lower limit, since our MI potentially entrap an already partially degassed melt (see above). Also, the model is intrinsically simplistic as it assumes a homogeneous (with fixed C content) mantle, while we know the mantle is in fact spatially heterogenous. In spite of these limitations, we conclude our results unambiguously prove the CO_2-rich nature of alkali-rich mafic melts feeding intraplate volcanism

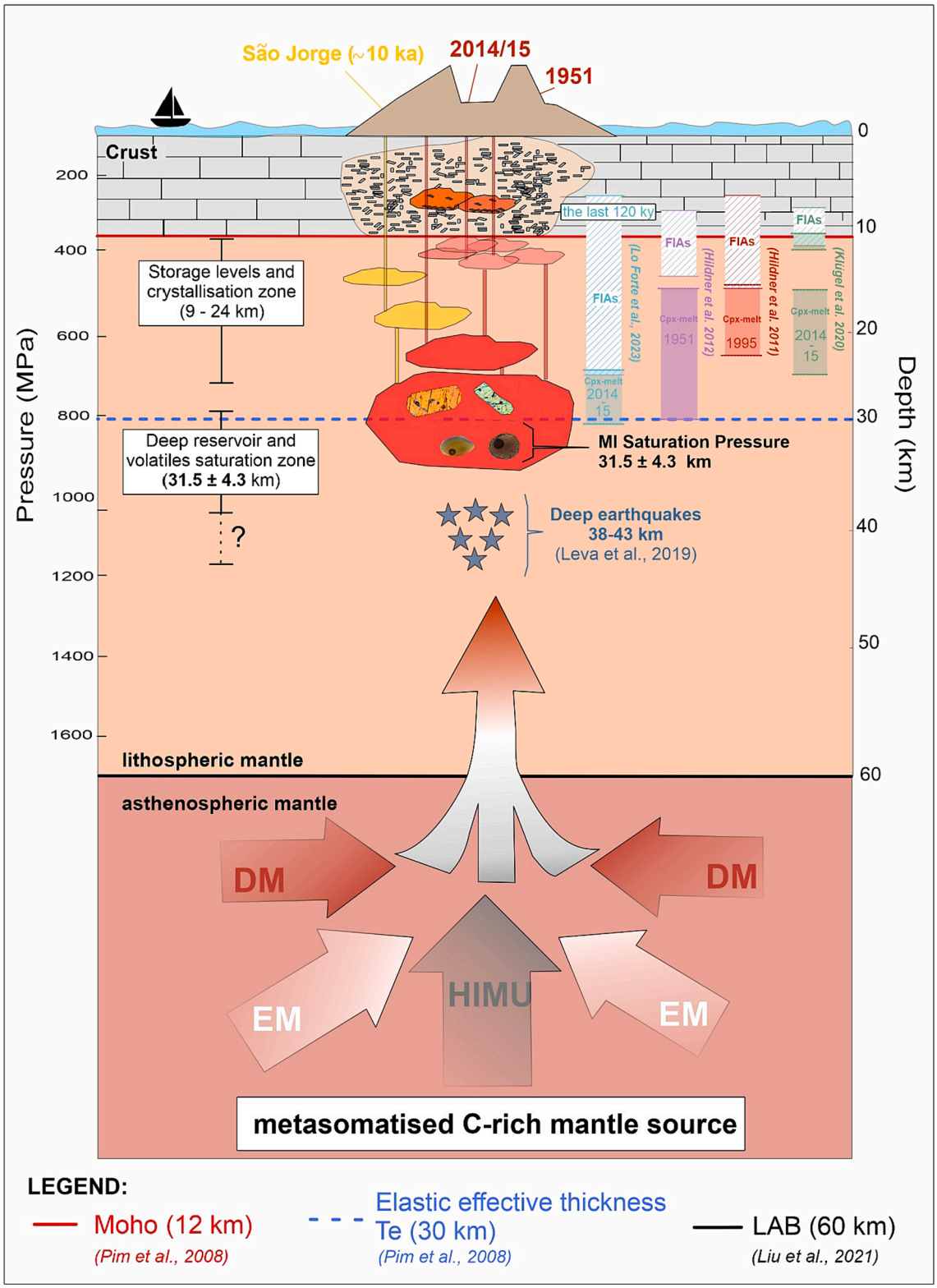

Fig. 11. Schematic cross-section (not to scale) showing the entire magma plumbing system of Fogo volcano. The model is based on the framework proposed by Lo Forte et al. (2023). Our data provide new constrain on the location of the roots of the volcano at 31.5 ± 4.3 km depth, which feed the upward magma storage zone at 13–25 km depth, as well as the magma stagnation zone located at 9–12 km depth. The blue stars represent the deep earthquakes recorded by Leva et al. (2019), in proximity of the deep magma accumulation zone. The right-hand side boxes present the previous barometry results. Consistent with Liu et al. (2021), the lithosphere-asthenosphere boundary (LAB) is located at 60 km depth. The three isotopic mantle components, which sign the magmatism of Cape Verde, were obtained from prior literature works (e.g., Gerlach et al., 1988; Doucelance et al., 2003; Escrig et al., 2005; Martins et al., 2010; Jackson et al., 2018a).

at Cape Verde. Note that, given the very low D for CO_2 (~0; Rosenthal et al., 2015), the use of a fractional meting equation (in place of batch melting) would not lead to any obvious difference.

Our results, combined with recent observations at other OIB localities globally (e.g., Anderson and Poland, 2017; Longprè et al., 2017; Boudoire et al., 2018; Hauri et al., 2018; Miller et al., 2019; Taracsák et al., 2019; Tucker et al., 2019), suggest that a C enriched OIB mantle source is likely to be the rule rather than the exception. Our estimated Fogo mantle content (355–414 ppm C) is well within the OIB mantle source range recently derived by Sun and Dasgupta (2023) (330–400 ppm), but well above the maximal C content of 164 ± 55 ppm inferred by Rosenthal et al. (2015) for the mantle source of intraplate basalts.

This carbon-enriched nature of global OIB, and of their mantle sources, has important consequences for our understanding of the mass/volume of deep carbon reservoirs, and of the deep carbon cycle - the transfer of carbon from the deep reservoir(s) (mantle + core) to the exosphere (ocean + atmosphere). First, our results contribute to the still open debate on the carbon content of the Bulk Silicate Earth, for which available estimates remain divergent, from ~110 ppm C (Hirschmann, 2018) to 330–450 ppm C (Marty et al., 2020) or even up to ~500 ppm C (Marty, 2012). The high C content of the OIB source mantle manifestly leans toward estimates based upon Ar (Marty, 2012) or C/N ratio (Marty et al., 2020) terrestrial inventories that require the deep convecting mantle to be C-rich, possibly > 10 more enriched than the Depleted Mantle (DMM) that sustains MORB volcanism (~20–56 ppm C; Voyer et al., 2017; Hauri et al., 2019). We need to bear in mind, however, that radiogenic isotopes have clearly proven the presence of a variety of recycled (slab-related) crustal materials in the OIB mantle (e.g., Hofmann and White, 1982; Hofmann et al., 1997; Hoernle et al., 2002; Cabral et al., 2013; Ellam, 2021), and that it is therefore well possible that a substantial fraction of the high C in OIB is in fact derived from a recycled crustal carbon source (Cabral et al., 2014). Carbon isotope results for OIB magmas would be vital to test this hypothesis but are unfortunately available for only a handful set of OIB. Where available, however, results suggest a heavy (crustal) carbon signature in the mantle (Sandoval-Velasquez et al., 2021). This implies that high carbon OIB may in fact reflect local infiltration of C-enriched metasomatic fluids/melts resulting from melting of carbonated lithologies (e.g., carbon-rich sediments and/or carbonated oceanic lithosphere) entrained into the mantle during past subduction events (Dasgupta, 2018). Such a situation may indeed explain the enriched nature of Fogo magmas.

Secondly, our results with those recently obtained elsewhere (Boudoire et al., 2018; Taracsák et al., 2019) are critical to refining estimates of the OIB contribution to deep carbon flux to the atmosphere. Previous work (Dasgupta and Hirschmann, 2010; Hauri et al., 2019) has found carbon outgassing from our planet interior to be primarily controlled by the volumetrically dominant MORB volcanism, and by less voluminous but more C-rich calcalkaline volcanism. However, MORB magmas are CO_2-poor (typically ≪0.1 wt%; see Fig. 10), while calcalkaline magma CO_2 contents lie somewhere between 0.1 and 1 wt% CO_2 (Plank and Manning, 2019). If the majority of OIB is as C-rich as Fogo, OIB volcanism is expected to contribute disproportionally (relative to other forms of volcanism) to the deep carbon flux to the atmosphere. Previous inventories (Dasgupta and Hirschmann, 2010) have found the carbon flux through OIB volcanism to be highly difficult to estimate, reflecting the often degassed (C-depleted) nature of OIB-carried MI (especially when no correction for shrinkage bubbles CO_2 is applied), and because of their extreme heterogeneity (in terms of depleted vs. enriched compositions). Because of these complexities, Dasgupta and Hirschmann (2010) conservatively derived their OIB carbon flux (1.2–30 Tg/yr) by assuming it to be ~10–50 % of the MORB C flux. If for simplicity we assume global OIB to be dominantly alkaline in nature and to contain 2.15 wt% CO_2 as our Fogo parental melt, then with a cumulative OIB magma extrusive output of 0.3–0.4 km^3/yr (Crisp, 1984) the global OIB carbon flux would be 16–21 Tg/yr, and > 100 Tg/yr if degassing of intrusive magma (1.5–2 km^3/yr; Crisp, 1984) is also taken into account.

These initial calculations are subject to large uncertainties. For example, tholeiitic OIB (e.g., Hawaii) or near-ridge hot-spot related OIB (e.g., Iceland) are less CO_2-poor than alkali rich OIB (Fig. 10), and the fact that all alkali rich OIB are as C-rich as Fogo (or El Hierro; Taracsák et al., 2019) is virtually untested. Ultimately, the volumetric proportions of enriched and non-enriched OIB would need to be constrained with a reasonable level of detail. Thus, our calculations here tentatively indicate that the global OIB carbon flux might be significantly higher than previously thought.

6. Conclusions

Olivine-hosted MI from recent (≤10 ka) Fogo basanitic tephra samples exhibit some of the highest (glass + bubbles) CO_2 contents (up to 2.15 wt%) on record. The Fogo MI are also found to additionally contain up to 2.73 wt% H_2O, 8205 ppm S, 1459 ppm Cl and 2249 ppm F. Our results are based on the use of three independent methodologies to correct for CO_2 contained in shrinkage bubbles, whose general agreement corroborates our reconstructed total CO_2 concentrations. The inferred MI CO_2/Nb (277–283) and CO_2/Ba (26–22) ratios are lower than the characteristic mantle ratios, suggesting our MI – although exceptionally CO_2-rich - do still underestimate the real CO_2 contents in primary melts (potentially containing up to 8–9 wt% CO_2; Sun and Dasgupta, 2023) due to pre-entrapment CO_2 loss to bubbles. This notwithstanding, our results suggest that the basanitic magmas sustaining Fogo activity may originate from a metasomatized, carbon-rich mantle source containing a minimum of 355–414 ppm C, in agreement with recent estimates for global OIB mantle sources. Prior to eruption, these parental basanitic magmas would remain stored in the lithospheric mantle in the ~27 to ~36 km depth range, deeper than previously inferred (Hildner et al., 2011, 2012; Klügel et al., 2020; Lo Forte et al., 2023).

Our results demonstrate the importance of measuring shrinkage bubble CO_2 to correctly reconstructing the architecture of magmatic plumbing systems, and confirm the exceptional carbon-rich signature of alkali rich OIB magmas and their carbon-rich mantle sources. In spite of their relatively low eruptive volumes, OIB eruptions may contribute disproportionally to global volcanic carbon outgassing from the mantle into the Earth's atmosphere. We tentatively estimate the global OIB carbon flux to potentially be as high as 17–23 Tg/yr.

7. Data availability

Data are available through Mendeley Data at: https://data.mendeley.com/datasets/gr2dy9grdn/2.

CRediT authorship contribution statement

Francesco Maria Lo Forte: Writing – review & editing, Writing – original draft, Visualization, Software, Methodology, Investigation, Data curation, Conceptualization. **Federica Schiavi:** Writing – original draft, Software, Methodology, Data curation, Conceptualization. **Estelle F. Rose-Koga:** Visualization, Validation, Methodology, Data curation. **Silvio G. Rotolo:** Visualization, Validation, Methodology, Conceptualization. **Maximilien Verdier-Paoletti:** Visualization, Software, Methodology, Data curation. **Alessandro Aiuppa:** Writing – review & editing, Writing – original draft, Visualization, Validation, Supervision, Project administration, Methodology, Funding acquisition, Formal analysis, Conceptualization. **Vittorio Zanon:** Writing – original draft, Supervision, Project administration, Methodology, Investigation, Funding acquisition, Data curation, Conceptualization.

Declaration of competing interest

The authors declare that they have no known competing financial

interests or personal relationships that could have appeared to influence the work reported in this paper.

Acknowledgements

This study was funded by the Deep Carbon Observatory (Alfred P. Sloan Foundation, USA), the Ministero dell'Università e Ricerca (Italy, Grants n. 2017LMNLAW and 2022HA8XCS), and Fundação para a Ciência e Tecnologia, Portugal (MAGAT project, ref. CIRCNA/OCT/0016/2019). LMV and IVAR are acknowledged for providing Francesco Maria Lo Forte access to laboratories. Dr. Jean-Luc Devidal (LMV) is acknowledged for assistance during electron probe analyses. Guilherme Bettencourt (IVAR) helped during sampling fieldwork at Fogo. The authors wish to acknowledge constructive comments from the Editor (Jeffrey G. Catalano), the Associate Editor (Adreas Stracke), M. Portnyagin, and one anonymous reviewer.

Appendix A. Supplementary material

The Supplementary Material comprises an excel file labelled as Supplementary Material S1, containing multiple sheets with detailed data information: Whole rock; Sample ubication; Host olivine analysis; Scoria analysis; Uncorrected MIs analysis; Corrected MIs analysis; Total MI CO_2 contents; MI Saturation Pressures. Additionally, there is a .pdf file labelled as Supplementary Material S2, which includes the calibration of nano-SIMS standards (Figure S1) and the Raman tomography of MI Fog 43-6-2 (Figure S2).

Supplementary material to this article can be found online at https://doi.org/10.1016/j.gca.2024.01.016.

References

Aiuppa, A., Moretti, R., Federico, C., Giudice, G., Gurrieri, S., Liuzzo, M., Papale, P., Shinohara, H., Valenza, M., 2007. Forecasting Etna eruptions by real-time observation of volcanic gas composition. Geol. 35, 1115.

Aiuppa, A., Bertagnini, A., Métrich, N., Moretti, R., Di Muro, A., Liuzzo, M., Tamburello, G., 2010. A model of degassing for Stromboli volcano. Earth and Planet. Sci. Lett. 295, 195–204.

Aiuppa, A., Bitetto, M., Francofonte, V., Velasquez, G., Parra, C.B., Giudice, G., et al., 2017. A CO_2-gas precursor to the March 2015 Villarrica volcano eruption. Geochem. Geophys. Geosyst. 18, 2120–2132.

Aiuppa, A., Ronchi, A., Bitetto, M., Rizzo, A.L., Viveiros, F., Allard, P., Frezzotti, M.L., Valenti, V., Zanon, V., 2020. The fumarolic CO_2 output from Pico do Fogo volcano (Cape Verde). Ital. J. Geosci. 139, 325–340.

Aiuppa, A., Casetta, F., Coltorti, M., Stagno, V., Tamburello, G., 2021. Carbon concentration increases with depth of melting in Earth's upper mantle. Nat. Geosci. 14, 697–703.

Aiuppa, A., Allard, P., Bernard, B., Lo Forte, F.M., Moretti, R., Hidalgo, S., 2022. Gas Leakage from Shallow Ponding Magma and Trapdoor Faulting at Sierra Negra Volcano (Isabela Island, Galápagos). Geochem. Geophys. Geosyst. 23.

Anderson, A.T., 1974. Evidence for a Picritic, Volatile-rich Magma beneath Mt. J. Petrol. 15, 243–267.

Anderson, K.R., Poland, M.P., 2017. Abundant carbon in the mantle beneath Hawaii. Nat. Geosci. 10, 704–708.

Ariskin, A.A., Barmina, G.S., 1999. An empirical model for the calculation of spinel-melt equilibria in mafic igneous systems at atmospheric pressure: 2. Fe-Ti Oxides. Contrib. Mineral. Petrol. 134, 251–263.

Aster, E.M., Wallace, P.J., Moore, L.R., Watkins, J., Gazel, E., Bodnar, R.J., 2016. Reconstructing CO_2 concentrations in basaltic melt inclusions using Raman analysis of vapor bubbles. J. Volcanol. Geotherm. Res. 323, 148–162.

Bali, E., Hartley, M.E., Halldórsson, S.A., Gudfinnsson, G.H., Jakobsson, S., 2018. Melt inclusion constraints on volatile systematics and degassing history of the 2014–2015 Holuhraun eruption. Iceland. Contrib. Mineral. Petrol. 173, 9.

Bamber, E.C., La Spina, G., Arzilli, F., de' Michieli Vitturi, M., Polacci, M., Hartley, M.E., et al., 2022. Basaltic Plinian eruptions at Las Sierras-Masaya volcano driven by cool storage of crystal-rich magmas. Commun. Earth Environ. 3, 253.

Blundy, J., Cashman, K., 2005. Rapid decompression-driven crystallization recorded by melt inclusions from Mount St. Helens Volcano. Geol. 33, 793.

Bonadiman, C., Beccaluva, L., Coltorti, M., Siena, F., 2005. Kimberlite-like Metasomatism and 'Garnet Signature' in Spinel-peridotite Xenoliths from Sal, Cape Verde Archipelago: relics of a subcontinental mantle domain within the atlantic oceanic lithosphere? J. Petrol. 46, 2465–2493.

Boudoire, G., Rizzo, A.L., Di Muro, A., Grassa, F., Liuzzo, M., 2018. Extensive CO_2 degassing in the upper mantle beneath oceanic basaltic volcanoes: First insights from Piton de la Fournaise volcano (La Réunion Island). Geochim. Et Cosmochim. Acta 235, 376–401.

Boudoire, G., Pasdeloup, G., Schiavi, F., Cluzel, N., Rafflin, V., Grassa, F., et al., 2023. Magma storage and degassing beneath the youngest volcanoes of the Massif Central (France): lessons for the monitoring of a dormant volcanic province. Chem Geol. 634, 121603.

Boulanger, M., France, L., 2023. Cumulate Formation and Melt Extraction from Mush-Dominated Magma Reservoirs: The Melt Flush Process Exemplified at Mid-Ocean Ridges. J. Petrol. 64, egad005.

Boulard, E., Menguy, N., Auzende, A.L., Benzerara, K., Bureau, H., Antonangeli, D., et al., 2012. Experimental Investigation of the Stability of Fe-Rich Carbonates in the Lower Mantle. J. Geophys. Res. 117, B02208.

Burgisser, A., Alletti, M., Scaillet, B., 2015. Simulating the behavior of volatiles belonging to the C-O–H–S system in silicate melts under magmatic conditions with the software D-Compress. Comput. Geosci. 79, 1–14.

Burton, M., Aiuppa, A., Allard, P., Asensio-Ramos, M., Confrades, A.P., La Spina, A., et al., 2023. Exceptional eruptive CO_2 emissions from intra-plate alkaline magmatism in the Canary volcanic archipelago. Commun. Earth Environ. 4, 467.

Buso, R., Laporte, D., Schiavi, F., Cluzel, N., Fonquernie, C., 2022. High-pressure homogenization of olivine-hosted CO_2-rich melt inclusions in a piston cylinder: insight into the volatile content of primary mantle melts. Eur. J. Mineral. 34, 325–349.

Cabral, R.A., Jackson, M.G., Rose-Koga, E.F., Koga, K.T., Whitehouse, M.J., Antonelli, M. A., et al., 2013. Anomalous sulphur isotopes in plume lavas reveal deep mantle storage of Archaean crust. Nature 496, 490–493.

Cabral, R.A., Jackson, M.G., Koga, K.T., Rose-Koga, E.F., Hauri, E.H., Whitehouse, M.J., et al., 2014. Volatile cycling of H_2O, CO_2, F, and Cl in the HIMU mantle: A new window provided by melt inclusions from oceanic hot spot lavas at Mangaia, Cook Islands. Geochem. Geophys. Geosyst. 15, 4445–4467.

Cannatelli, C., Doherty, A.L., Esposito, R., Lima, A., De Vivo, B., 2016. Understanding a volcano through a droplet: A melt inclusion approach. J. of Geochem. Explor. 171, 4–19.

Cartigny, P., Pineau, F., Aubaud, C., Javoy, M., 2008. Towards a consistent mantle carbon flux estimate: Insights from volatile systematics (H_2O/Ce, δD, CO_2/Nb) in the North Atlantic mantle (14° N and 34° N). Earth and Planet. Sci. Lett. 265, 672–685.

Chen, Y., Provost, A., Schiano, P., Cluzel, N., 2011. The rate of water loss from olivine-hosted melt inclusions. Contrib. Mineral. Petrol. 162 (3), 625–636.

Cottrell, E., Spiegelman, M., Langmuir, C.H., 2002. Consequences of diffusive reequilibration for the interpretation of melt inclusions: reequilibration of melt inclusions. Geochem. Geophys. Geosyst. 3, 1–26.

Créon, L., Levresse, G., Remusat, L., Bureau, H., Carrasco-Nuñez, G., 2018. New method for initial composition determination of crystallized silicate melt inclusions. Chem. Geol. 483, 162–173.

Crisp, J.A., 1984. Rates of magma emplacement and volcanic output. J. Volcanol. Geotherm. Res. 20, 177–211.

Danyushevsky, L.V., 2001. The effect of small amounts of H_2O on crystallisation of mid-ocean ridge and backarc basin magmas. J. Volcanol. and Geother. Res. 110, 265–280.

Danyushevsky, L.V., McNeill, A.W., Sobolev, A.V., 2002. Experimental and petrological studies of melt inclusions in phenocrysts from mantle-derived magmas: an overview of techniques, advantages and complications. Chem. Geol. 183, 5–24.

Danyushevsky, L.V., Plechov, P., 2011. Petrolog 3: Integrated software for modeling crystallization processes: Petrolog3. Geochem. Geophys. Geosyst. 12.

Danyushevsky, L.V., Della-Pasqua, F.N., Sokolov, S., 2000. Re-equilibration of melt inclusions trapped by magnesian olivine phenocrysts from subduction-related magmas: petrological implications. Contrib. Mineral. Petrol. 138, 68–83.

Dasgupta, R., 2018. Volatile-bearing partial melts beneath oceans and continents – where, how much, and of what compositions? Am. J. Sci. 318, 141–165.

Dasgupta, R., Hirschmann, M.M., 2010. The deep carbon cycle and melting in Earth's interior. Earth and Planet. Sci. Lett. 298, 1–13.

Dasgupta, R., Chi, H., Shimizu, N., Buono, A.S., Walker, D., 2013. Carbon solution and partitioning between metallic and silicate melts in a shallow magma ocean: implications for the origin and distribution of terrestrial carbon. Geochim. Cos-Mochim. Acta 102, 191–212.

Day, S.J., Heleno da Silva, S.I.N., Fonseca, J.F.B.D., 1999. A past giant lateral collapse and present-day flank instability of Fogo, Cape Verde Islands. J. Volcanol. and Geother. Res. 94, 191–218.

Dayton, K., Gazel, E., Wieser, P., Troll, V.R., Carracedo, J.C., La Madrid, H., et al., 2023. Deep magma storage during the 2021 La Palma eruption. Sci. Adv. 9, 6.

de Moor, J.M., Aiuppa, A., Avard, G., Wehrmann, H., Dunbar, N., Muller, C., et al., 2016. Turmoil at Turrialba Volcano (Costa Rica): Degassing and eruptive processes inferred from high-frequency gas monitoring: Turmoil at Turrialba Volcano. J. Geophys. Res. Solid Earth 121, 5761–5775.

DeVitre, C.L., Gazel, E., Ramalho, R.S., Venugopal, S., Steele-MacInnis, M., Hua, J., et al., 2023. Oceanic intraplate explosive eruptions 1102 fed directly from the mantle. Proc. Natl. Acad. Sci. 120 (33), e2302093120.

Di Martino, C., Forni, F., Frezzotti, M.L., Palmeri, R., Webster, J.D., Ayuso, R.A., et al., 2011. Formation of cordierite-bearing lavas during anatexis in the lower crust beneath Lipari Island (Aeolian arc, Italy). Contrib. Mineral. Petrol. 162, 1011–1030.

Di Muro, A., Metrich, N., Vergani, D., Rosi, M., Armienti, P., Fougeroux, T., Deloule, E., Arienzo, I., Civetta, L., 2014. The Shallow Plumbing System of Piton de la Fournaise Volcano (La Reunion Island, Indian Ocean) Revealed by the Major 2007 Caldera-Forming Eruption. J. Petrol. 55, 1287–1315.

Dixon J.E. and Stolper E.M., 1995. An Experimental Study of Water and Carbon Dioxide Solubilities in Mid-Ocean Ridge Basaltic Liquids. Part II: Applications to Degassing. J. Petrol. 36,6,1633-1646.

Doucelance, R., Escrig, S., Moreira, M., Gariépy, C., Kurz, M.D., 2003. Pb-Sr-He isotope and trace element geochemistry of the Cape Verde Archipelago. Geochim. Cosmochim. Acta 67, 3717–3733.
Edmonds, M., Aiuppa, A., Humphreys, M., Moretti, R., Giudice, G., Martin, R.S., et al., 2010. Excess volatiles supplied by mingling of mafic magma at an andesite arc volcano: excess volatiles supplied by underplating. Geochem. Geophys. Geosyst. 11.
Edmonds, M., Wallace, P.J., 2017. Volatiles and Exsolved Vapor in Volcanic Systems. Elements 13, 29–34.
Eguchi, J., Dasgupta, R., 2018. A CO_2 solubility model for silicate melts from fluid saturation to graphite or diamond saturation. Chem. Geol. 487, 23–38.
Ellam, R.M., 2021. Radiogenic isotopes and mantle evolution. In: Alderton, D., Elias, S.A. (Eds.), Encyclopedia of Geology. Academic Press, Amsterdam, pp. 330–344.
Escrig, S., Doucelance, R., Moreira, M., Allègre, C.J., 2005. Os isotope systematics in Fogo Island: Evidence for lower continental crust fragments under the Cape Verde Southern Islands. Chem. Geol. 219, 93–113.
Esposito, R., Bodnar, R.J., Danyushevsky, L., De Vivo, B., Fedele, L., Hunter, J., Lima, A., Shimizu, N., 2011. Volatile evolution of magma associated with the Solchiaro Eruption in the Phlegrean Volcanic District (Italy). Journal of Petrology. 52, 2431–2460.
Esposito, R., Lamadrid, H.M., Redi, D., Steele-MacInnis, M., Bodnar, R.J., Manning, C.E., De Vivo, B., Cannatelli, C., Lima, A., 2016. Detection of liquid H_2O in vapor bubbles in reheated melt inclusions: Implications for magmatic fluid composition and volatile budgets of magmas? Am. Mineral. 101, 1691–1695.
Fall, A., Bodnar, R.J., Szabó, C., Pál-Molnár, E., 2007. Fluid evolution in the nepheline syenites of the Ditrău alkaline Massif, Transylvania, Romania. Lithos 95, 331–345.
Feignon, J.G., Cluzel, N., Schiavi, F., Moune, S., Roche, O., Clavero, J., et al., 2022. High CO_2 content in magmas of the explosive andesitic Enco eruption of Mocho-Choshuenco volcano (Chile). Bull. Volcanol. 84, 40.
Foeken, J.P.T., Day, S., Stuart, F.M., 2009. Cosmogenic ^{3}He exposure dating of the Quaternary basalts from Fogo, Cape Verdes: Implications for rift zone and magmatic reorganisation. Quaternary Geochronology 4, 37–49.
Foley, S.F., 2011. A Reappraisal of Redox Melting in the Earth's Mantle as a Function of Tectonic Setting and Time. J. Petrol. 52 (7–8), 1363–1391.
Foley, S.F., Fischer, T.P., 2017. An essential role for continental rifts and lithosphere in the deep carbon cycle. Nat. Geosci. 10, 897–902.
Foley, S.F., Yaxley, G.M., Rosenthal, A., Buhre, S., Kiseeva, E.S., Rapp, R.P., Jacob, D.E., 2009. The composition of near-solidus melts of peridotite in the presence of CO_2 and H_2O between 40 and 60 kbar. Lithos. 112S, 274–283.
Foley, S.F., Link, K., Tiberindwa, J.V., Barifaijo, E., 2012. Patterns and origin of igneous activity around the Tanzanian craton. J. Afr. Earth Sci. 62, 1–18.
French, S., Romanowicz, B., 2015. Broad plumes rooted at the base of the Earth's mantle beneath major hotspots. Nature 525, 95–99.
Gaetani, G.A., Watson, E.B., 2002. Modeling the major-element evolution of olivine-hosted melt inclusions. Chem. Geol. 183, 25–41.
Gaetani, G.A., O'Leary, J.A., Shimizu, N., Bucholz, C.E., Newville, M., 2012. Rapid reequilibration of H_2O and oxygen fugacity in olivine-hosted melt inclusions. Geol. 40 (10), 915–918.
Gaetani, G.A., Watson, E.B., 2000. Open system behavior of olivine-hosted melt inclusions. Earth and Planet. Sci. Lett. 183, 27–41.
Gerlach, D.C., Cliff, R.A., Davies, G.R., Norry, M., Hodgson, N., 1988. Magma sources of the Cape Verdes archipelago: Isotopic and trace element constraints. Geochim. Et Cosmochim. Acta 52, 2979–2992.
Ghiorso, M.S., Gualda, G.A.R., 2015. An H_2O–CO_2 mixed fluid saturation model compatible with rhyolite-MELTS. Contrib. Mineral. Petrol. 169, 53.
Giordano, D., Nichols, A.R., Dingwell, D.B., 2005. Glass transition temperatures of natural hydrous melts: a relationship with shear viscosity and implications for the welding process. J. Volcanol. and Geother. Res. 142 (1–2), 105–118.
Guzmics, T., Berkesi, M., Bodnar, R.J., Fall, A., Bali, E., Milke, R., Vetlényi, E., Szabó, C., 2019. Natrocarbonatites: A hidden product of three-phase immiscibility. Geol. 47, 527–530.
Halldórsson, S.A., Marshall, E.W., Caracciolo, A., Matthews, S., Bali, E., Rasmussen, M.B., et al., 2022. Rapid shifting of a deep magmatic source at Fagradalsfjall volcano, Iceland. Nature 609, 529–534.
Hartley, M.E., Maclennan, J., Edmonds, M., Thordarson, T., 2014. Reconstructing the deep CO_2 degassing behaviour of large basaltic fissure eruptions. Earth and Planet. Sci. Lett. 393, 120–131.
Hauri, E., 2002. SIMS analysis of volatiles in silicate glasses, 2: isotopes and abundances in Hawaiian melt inclusions. Chem. Geol. 183, 115–141.
Hauri, E.H., Maclennan, J., McKenzie, D., Gronvold, K., Oskarsson, N., Shimizu, N., 2018. CO_2 content beneath northern Iceland and the variability of mantle carbon. Geol. 46, 55–58.
Hauri, E.H., Cottrell, E., Kelley, K.A., Tucker, J.M., Shimizu, K., Voyer, M.L., Marske, J., Saal, A.E., 2019. Carbon in the Convecting Mantle. In: Orcutt, B.N., Daniel, I., Dasgupta, R. (Eds.), Deep Carbon. Cambridge University Press, pp. 237–275.
Heath, E., Macdonald, R., Belkin, H., Hawkesworth, C., Sigurdsson, H., 1998. Magma genesis at Soufriere Volcano, St Vincent, Lesser Antilles Arc. J. Petrol. 39, 1721–1764.
Hildner, E., Klügel, A., Hauff, F., 2011. Magma storage and ascent during the 1995 eruption of Fogo, Cape Verde Archipelago. Contrib. Mineral. Petrol. 162, 751–772.
Hildner, E., Klügel, A., Hansteen, T.H., 2012. Barometry of lavas from the 1951 eruption of Fogo, Cape Verde Islands: Implications for historic and prehistoric magma plumbing systems. J. Volcanol. and Geother. Res. 217–218, 73–90.
Hirschmann, M.M., 2006. Water, melting, and the deep Earth H2O cycle Annu. Rev. Earth Planet. Sci. 629–653.
Hirschmann, M.M., 2018. Comparative deep Earth volatile cycles: The case for C recycling from exosphere/mantle fractionation of major (H_2O, C, N) volatiles and from H_2O/Ce, CO_2/Ba, and CO_2/Nb exosphere ratios. Earth and Planet. Sci. Lett. 502, 262–273.
Hoernle, K., Tilton, G., Le Bas, M.J., Duggen, S., Garbe-Schönberg, D., 2002. Geochemistry of oceanic carbonatites compared with continental carbonatites: mantle recycling of oceanic crustal carbonate. Contrib. Mineral. Petrol. 142, 520–542.
Hofmann, A.W., 1997. Mantle geochemistry: the message from oceanic volcanism. Nature 385, 219–229.
Hofmann, A.W., White, W.M., 1982. Mantle plumes from ancient oceanic crust Earth Planet. Sci. Lett. 57 (2), 421–436.
Holm, P.M., Wilson, J.R., Christensen, B.P., Hansen, L., Hansen, S.L., Hein, K.M., et al., 2006. Sampling the Cape Verde Mantle Plume: Evolution of Melt Compositions on Santo Antão, Cape Verde Islands. J. Petrol. 47 (1), 145–189.
Hudgins, T.R., Mukasa, S.B., Simon, A.C., Moore, G., Barifaijo, E., 2015. Melt inclusion evidence for CO_2-rich melts beneath the western branch of the East African Rift: implications for long-term storage of volatiles in the deep lithospheric mantle Contrib. Mineral. Petrol. 169, 1–18.
Iacono-Marziano, G., Morizet, Y., Le Trong, E., Gaillard, F., 2012. New experimental data and semi-empirical parameterization of H_2O–CO_2 solubility in mafic melts. Geochim. Cosmochim. Acta 97, 1–23.
Iacovino, K., Matthews, S., Wieser, P.E., Moore, G.M., Bégué, F., 2021. VESIcal part I: An open-source thermodynamic model engine for mixed volatile (H_2O-CO_2) solubility in silicate melts. Earth Space Sci. 8, e2020EA001584.
Jackson, M.G., Becker, T.W., Konter, J.G., 2018. Evidence for a deep mantle source for EM and HIMU domains from integrated geochemical and geophysical constraints. Earth Planet. Sci. Lett. 484, 154–167.
Jiménez-Mejías, M., Andújar, J., Scaillet, B., Casillas, R., 2021. Experimental determination of H_2O and CO_2 solubilities of mafic alkaline magmas from Canary Islands. Comptes Rendus. Géoscience 353, 289–314.
Kamenetsky, V.S., Davidson, P., Mernagh, T.P., Crawford, A.J., Gemmell, J.B., Portnyagin, M.V., Shinjo, R., 2002. Fluid bubbles in melt inclusions and pillow-rim glasses: high-temperature precursors to hydrothermal fluids? Chem. Geol. 183, 349–364.
Kawakami, Y., Yamamoto, J., Kagi, H., 2003. Micro-Raman densimeter for CO_2 inclusions in mantle-derived minerals. Appl. Spectrosc. 57 (11), 1333–1339.
Kendrick, M.A., Jackson, M.G., Kent, A.J.R., Hauri, E.H., Wallace, P.J., Woodhead, J., 2014. Contrasting behaviours of CO_2, S, H_2O and halogens (F, Cl, Br, and I) in enriched-mantle melts from Pitcairn and Society seamounts. Chem. Geol. 370, 69–81.
Kent, A.J.R., 2008. Melt inclusions in basaltic and related volcanic rocks. Rev. Mineral. Geochem. 69 (1), 273–331.
Klügel, A., Day, S., Schmid, M., Faria, B., 2020. Magma Plumbing During the 2014–2015 Eruption of Fogo (Cape Verde Islands). Front. Earth Sci. 8, 157.
Koleszar, A.M., Saal, A.E., Hauri, E.H., Nagle, A.N., Liang, Y., Kurz, M.D., 2009. The volatile contents of the Galapagos plume; evidence for H_2O and F open system behavior in melt inclusions. Earth and Planet. Sci. Lett. 287, 442–452.
Le Voyer, M., Kelley, K.A., Cottrell, E., Hauri, E.H., 2017. Heterogeneity in mantle carbon content from CO_2-undersaturated basalts. Nat. Commun. 8, 14062.
Lesher, C.E., Spera, F.J., 2015. Thermodynamic and Transport Properties of Silicate Melts and Magma. The Encyclopedia of Volcanoes. Elsevier 113–141.
Liu, B., Zhang, Z., Giuliani, A., Xie, Q., Kong, W., Wang, C., et al., 2023. A Mantle Plume Connection for Alkaline Lamprophyres (Sannaites) from the Permian Tarim Large Igneous Province: Petrological, Geochemical and Isotopic Constraints. J. Petrol. 64, egad004.
Liu, X., Zhao, D., 2021. Seismic evidence for a plume-modified oceanic lithosphere–asthenosphere system beneath Cape Verde. Geophys. J. Int. 225, 872–886.
Lo Forte, F.M., Aiuppa, A., Rotolo, S.G., Zanon, V., 2023. Temporal evolution of the Fogo Volcano magma storage system (Cape Verde Archipelago): a fluid inclusions perspective. J. Volcanol. and Geother. Res. 433, 107730.
Longpré, M.-A., Stix, J., Klügel, A., Shimizu, N., 2017. Mantle to surface degassing of carbon- and sulphur-rich alkaline magma at El Hierro, Canary Islands. Earth and Planet. Sci. Lett. 460, 268–280.
Lowenstern, J.B., 2015. Bursting the bubble of melt inclusions. Am. Mineral. 100, 672–673.
Lowenstern, J.B., 1995. Applications of silicate-melt inclusions to the study of magmatic volatiles. Magmas, Fluids, and Ore Deposits. In: Thompson, J.F.H. (Ed.), MAC Short Course, vol. 23, pp. 71–100, Victoria, British Columbia.
Maclennan, J., 2017. Bubble formation and decrepitation control the CO_2 content of olivine-hosted melt inclusions: melt inclusion carbon dioxide. Geochem. Geophys. Geosyst. 18, 597–616.
Marini, L., Moretti, R., Accornero, M., 2011. Sulfur Isotopes in Magmatic-Hydrothermal Systems, Melts, and Magmas. Reviews in Mineralogy and Geochemistry 73, 423–492.
Martínez-Moreno, F.J., Monteiro Santos, F.A., Madeira, J., Pous, J., Bernardo, I., Soares, A., et al., 2018. Investigating collapse structures in oceanic islands using magnetotelluric surveys: The case of Fogo Island in Cape Verde. J. Volcanol. and Geother. Res. 357, 152–162.
Martins, S., Mata, J., Munhá, J., Mendes, M.H., Maerschalk, C., Caldeira, R., et al., 2010. Chemical and mineralogical evidence of the occurrence of mantle metasomatism by carbonate-rich melts in an oceanic environment (Santiago Island, Cape Verde). Miner. Petrol. 99, 43–65.
Marty, B., 2012. The origins and concentrations of water, carbon, nitrogen and noble gases on Earth. Earth Planet. Sci. Lett. 313, 56–66.
Marty, B., Almayrac, M., Barry, P.H., Bekaert, D.V., Broadley, M.W., Byrne, D.J., et al., 2020. An evaluation of the C/N ratio of the mantle from natural CO_2-rich gas

analysis: Geochemical and cosmochemical implications. Earth Planet. Sci. Lett. 551, 116574.
Massare, D., Métrich, N., Clocchiatti, R., 2002. High-temperature experiments on silicate melt inclusions in olivine at 1 atm: Inference on temperatures of homogenization and H_2O concentrations. Chem. Geol. 183 (1–4), 87–98.
Mata, J., Martins, S., Mattielli, N., Madeira, J., Faria, B., Ramalho, R.S., et al., 2017. The 2014–15 eruption and the short-term geochemical evolution of the Fogo volcano (Cape Verde): Evidence for small-scale mantle heterogeneity. Lithos 288–289, 91–107.
Melián, G.V., Hernández, P.A., Pérez, N.M., Asensio-Ramos, M., Padrón, E., Alonso, M., et al., 2021. Insights from Fumarole Gas Geochemistry on the Recent Volcanic Unrest of Pico do Fogo. Cape Verde. Front. Earth Sci. 9, 631190.
Métrich, N., Wallace, P.J., 2008. Volatile Abundances in Basaltic Magmas and Their Degassing Paths Tracked by Melt Inclusions. Reviews in Mineralogy and Geochemistry 69, 363–402.
Métrich, N., Clocchiatti, R., Mosbah, M., Chaussidon, M., 1993. The 1989–1990 activity of Etna magma mingling and ascent of H_2O, Cl, S rich basaltic magma. Evidence from melt inclusions. J. Volcanol. and Geother. Res. 59, 131–144.
Métrich, N., Allard, P., Aiuppa, A., Bani, P., Bertagnini, A., Shinohara, H., et al., 2011. Magma and Volatile Supply to Post-collapse Volcanism and Block Resurgence in Siwi Caldera (Tanna Island, Vanuatu Arc). J. of Petrol. 52, 1077–1105.
Métrich, N., Zanon, V., Créon, L., Hildenbrand, A., Moreira, M., Marques, F.O., 2014. Is the 'Azores Hotspot' a Wetspot? Insights from the Geochemistry of Fluid and Melt Inclusions in Olivine of Pico Basalts. J. Petrol. 55, 377–393.
Michael, P.J., Graham, D.W., 2015. The behavior and concentration of CO_2 in the suboceanic mantle: Inferences from undegassed ocean ridge and ocean island basalts. Lithos 236–237, 338–351.
Miller, W.G.R., Maclennan, J., Shorttle, O., Gaetani, G.A., Le Roux, V., Klein, F., 2019. Estimating the carbon content of the deep mantle with Icelandic melt inclusions. Earth Planet. Sci. Lett. 523, 115699.
Mironov, N.L., Portnyagin, M.V., 2011. H_2O and CO_2 in parental magmas of Kliuchevskoi volcano inferred from study of melt and fluid inclusions in olivine. Russian Geology and Geophysics 52, 1353–1367.
Mironov, N., Portnyagin, M., Botcharnikov, R., Gurenko, A., Hoernle, K., Holtz, F., 2015. Quantification of the CO_2 budget and H_2O–CO_2 systematics in subduction-zone magmas through the experimental hydration of melt inclusions in olivine at high H_2O pressure. Earth and Planetary Science Letters 425, 1–11.
Mironov, N., Tobelko, D.P., Smirnov, S.Z., Portnyagin, M.V., Krasheninnikov, S.P., 2020. Estimation of CO_2 content in the gas phase of melt inclusions using Raman spectroscopy: Case study of inclusions in olivine from the Karymsky volcano (Kamchatka). Russian Geology and Geophysics 61, 600–610.
Mitchell, M.A., Peacock, J.R., Burgess, S.D., 2023. Imaging the magmatic plumbing of the Clear Lake Volcanic Field using 3-D gravity inversions. J. Volcanol. and Geother. Res. 435, 107758.
Moore, L.R., Bodnar, R.J., 2019. A pedagogical approach to estimating the CO_2 budget of magmas. JGS 176, 398–407.
Moore, L.R., Gazel, E., Tuohy, R., Lloyd, A.S., Esposito, R., Steele-MacInnis, M., et al., 2015. Bubbles matter: An assessment of the contribution of vapor bubbles to melt inclusion volatile budgets. Am. Mineral. 100, 806–823.
Moore, L.R., Mironov, N., Portnyagin, M., Gazel, E., Bodnar, R.J., 2018. Volatile contents of primitive bubble-bearing melt inclusions from Klyuchevskoy volcano, Kamchatka: Comparison of volatile contents determined by mass-balance versus experimental homogenization. J. Volcanol. Geotherm. Res. 358, 124–131.
Moretti, R., Papale, P., Ottonello, G., 2003. A model for the saturation of C-O-H-S fluids in silicate melts. SP 213, 81–101.
Moretti, R., Arienzo, I., Civetta, L., Orsi, G., Papale, P., 2013a. Multiple magma degassing sources at an explosive volcano. Earth and Planet. Sci. Lett. 367, 95–104.
Moretti, R., Arienzo, I., Orsi, G., Civetta, L., D'Antonio, M., 2013b. The Deep Plumbing System of Ischia: a Physico-chemical Window on the Fluid-saturated and CO_2-sustained Neapolitan Volcanism (Southern Italy). J. Petrol. 54, 951–984.
Mourão, C., Moreira, M., Mata, J., Raquin, A., Madeira, J., 2012. Primary and secondary processes constraining the noble gas isotopic signatures of carbonatites and silicate rocks from Brava Island: evidence for a lower mantle origin of the Cape Verde plume. Contrib. Mineral. Petrol. 163, 995–1009.
Moussallam, Y., Georgeais, G., Rose-Koga, E.F., Koga, K.T., Hartley, M.E., Scaillet, B., et al., 2023. CO_2-undersaturated melt inclusions from the South West Indian Ridge record surprisingly uniform redox conditions. Geochem. Geophys. Geosyst. 24, e2023GC011235.
Moussallam, Y., Oppenheimer, C., Scaillet, B., Gaillard, F., Kyle, P., Peters, N., Hartley, M., Berlo, K., Donovan, A., 2014. Tracking the changing oxidation state of Erebus magmas, from mantle to surface, driven by magma ascent and degassing. Earth and Planet. Sci. Lett. 393, 200–209.
Moussallam, Y., Longpré, M.-A., McCammon, C., Gomez-Ulla, A., Rose-Koga, E.F., Scaillet, B., Peters, N., Gennaro, E., Paris, R., Oppenheimer, C., 2019. Mantle plumes are oxidised. Earth and Planet. Sci. Lett. 527, 115798.
Naumov, V.B., Portnyagin, M.V., Tolstykh, M.L., Yarmolyuk, V.V., 2003. Composition of Magmatic Melts from the Southern Baikal Volcanic Region: A Study of Inclusions in Olivine from Trachybasalts. Geochemistry International. 41, 213–223.
Newman, S., Lowenstern, J.B., 2002. VolatileCalc: a silicate melt–H_2O–CO_2 solution model written in Visual Basic for excel. Computers & Geosciences 28, 597–604.
Ni, P., Zhang, Y., Guan, Y., 2017. Volatile loss during homogenization of lunar melt inclusions. Earth and Planet. Sci. Lett. 478, 214–224.
Oppenheimer, C., Moretti, R., Kyle, P.R., Eschenbacher, A., Lowenstern, J.B., Hervig, R. L., Dunbar, N.W., 2011. Mantle to surface degassing of alkalic magmas at Erebus volcano. Antarctica. Earth and Planet. Sci. Lett. 306, 261–271.
Pérez, W., Freundt, A., Kutterolf, S., 2020. The basaltic plinian eruption of the ~6 ka San Antonio Tephra and formation of the Masaya caldera. Nicaragua. J. Volcanol. and Geother. Res. 401, 106975.
Pim, J., Peirce, C., Watts, A.B., Grevemeyer, I., Krabbenhoeft, A., 2008. Crustal structure and origin of the Cape Verde rise. Earth Planet. Sci. Lett. 272, 422–428.
Pino, N.A., Moretti, R., Allard, P., Boschi, E., 2011. Seismic precursors of a basaltic paroxysmal explosion track deep gas accumulation and slug upraise. J. Geophys. Res. 116, B02312.
Plank, T., Manning, C.E., 2019. Subducting carbon. Nature 574, 343–352.
Portnyagin, M., Almeev, R., Matveev, S., Holtz, F., 2008. Experimental evidence for rapid water exchange between melt inclusions in olivine and host magma. Earth and Planet. Sci. Lett. 272 (3), 541–552.
Portnyagin, M., Mironov, N., Botcharnikov, R., Gurenko, A., Almeev, R.R., Luft, C., et al., 2019. Dehydration of melt inclusions in olivine and implications for the origin of silica-undersaturated island-arc melts. Earth and Planet. Sci. Lett. 517, 95–105.
Portnyagin, M.V., Naumov, V.B., Mironov, N.L., Belousov, I.A., Kononkova, N.N., 2011. Composition and evolution of the melts erupted in 1996 at Karymskoe Lake, Eastern Kamchatka: Evidence from inclusions in minerals. Geochem. Int. 49, 1085–1110.
Putirka, K.D., Perfit, M., Ryerson, F.J., Jackson, M.G., 2007. Ambient and excess mantle temperatures, olivine thermometry, and active vs. passive upwelling. Chem. Geol. 241, 177–206.
Rasmussen, D.J., Plank, T.A., Roman, D.C., Power, J.A., Bodnar, R.J., Hauri, E.H., 2018. When does eruption run-up begin? Multidisciplinary insight from the 1999 eruption of Shishaldin volcano. Earth and Planet. Sci. Lett. 486, 1–14.
Rasmussen, D.J., Plank, T.A., Wallace, P.J., Newcombe, M.E., Lowenstern, J.B., 2020. Vapor-bubble growth in olivine-hosted melt inclusions. Am. Mineral. 105, 1898–1919.
Robidoux, P., Frezzotti, M.L., Hauri, E.H., Aiuppa, A., 2018. Shrinkage Bubbles: The C-O–H–S Magmatic Fluid System at San Cristóbal Volcano. J. Petrol. 59, 2093–2122.
Roedder, E., 1979. Origin and significance of magmatic inclusions. Bull. Mineral. 102, 467–510.
Romero, J.E., Morgado, E., Pisello, A., Boschetty, F., Petrelli, M., Cáceres, F., et al., 2023. Pre-eruptive Conditions of the 3 March 2015 Lava Fountain of Villarrica Volcano (Southern Andes). Bull. Volcanol. 85 (1), 2.
Rose-Koga, E.F., Koga, K.T., Devidal, J.-L., Shimizu, N., Le Voyer, M., Dalou, C., et al., 2020. In-situ measurements of magmatic volatile elements, F, S, and Cl, by electron microprobe, secondary ion mass spectrometry, and heavy ion elastic recoil detection analysis. Am. Mineral. 105, 616–626.
Rose-Koga, E.F., Bouvier, A.-S., Gaetani, G.A., Wallace, P.J., Allison, C.M., Andrys, J.A., et al., 2021. Silicate melt inclusions in the new millennium: A review of recommended practices for preparation, analysis, and data presentation. Chem. Geol. 570, 120145.
Rose-Koga, E.F., Koga, K.T., Schiano, P., Le Voyer, M., Shimizu, N., Whitehouse, M.J., et al., 2012. Mantle source heterogeneity for south tyrrhenian magmas revealed by Pb isotopes and halogen contents of olivine-hosted melt inclusions. Chem. Geol. 334, 266–279.
Rosenthal, A., Hauri, E.H., Hirschmann, M.M., 2015. Experimental determination of C, F, and H partitioning between mantle minerals and carbonated basalt, CO_2/Ba and CO_2/Nb systematics of partial melting, and the CO_2 contents of basaltic source regions. Earth and Planet. Sci. Lett. 412, 77–87.
Rowe, M.C., Peate, D.W., Ukstins Peate, I., 2011. An Investigation into the Nature of the Magmatic Plumbing System at Paricutin Volcano. Mexico. J. Petrol. 52, 2187–2220.
Saal, A.E., Hauri, E.H., Langmuir, C.H., Perfit, M.R., 2002. Vapour undersaturation in primitive mid-ocean-ridge basalt and the volatile content of Earth's upper mantle. Nature 419, 451–455.
Sadofsky, S.J., Portnyagin, M., Hoernle, K., 2008. Subduction cycling of volatiles and trace elements through the Central American volcanic arc: evidence from melt inclusions. Contrib. Mineral. Petrol. 155, 433–456.
Sandoval-Velasquez, A., Rizzo, A.L., Aiuppa, A., Remigi, S., Padrón, E., Pérez, N.M., et al., 2021. Recycled crustal carbon in the depleted mantle source of El Hierro volcano, Canary Islands. Lith. 400–401, 106414.
Schiano, P., 2003. Primitive mantle magmas recorded as silicate melt inclusions in igneous minerals. Earth-Sci. Rev. 63, 121–144.
Schiavi, F., Bolfan-Casanova, N., Buso, R., Laumonier, M., Laporte, D., Medjoubi, K., Venugopal, S., Gómez-Ulla, A., Cluzel, N., Hardiagon, M., 2020. Quantifying magmatic volatiles by Raman microtomography of glass inclusion-hosted bubbles. Geochem. Persp. Let. 16, 17–24.
Sharpe, M.S., Barker, S.J., Rooyakkers, S.M., Wilson, C.J.N., Chambefort, I., Rowe, M.C., Schipper, C.I., Charlier, B.L.A., 2022. A sulfur and halogen budget for the large magmatic system beneath Taupō volcano. Contrib. Mineral. Petrol. 177, 95.
Shaw, D.M., 1970. Trace element fractionation during anatexis. Geochimica Et Cosmochimica Acta 34, 237–243.
Shaw, A.M., Hauri, E.H., Fischer, T.P., Hilton, D.R., Kelley, K.A., 2008. Hydrogen isotopes in Mariana arc melt inclusions: Implications for subduction dehydration and the deep-Earth water cycle. Earth and Planet. Sci. Lett. 275, 138–145.
Shaw, A.M., Behn, M.D., Humphris, S.E., Sohn, R.A., Gregg, P.M., 2010. Deep pooling of low degree melts and volatile fluxes at the 85°E segment of the Gakkel Ridge: Evidence from olivine-hosted melt inclusions and glasses. Earth and Planet. Sci. Lett. 289, 311–322.
Shimizu, K., Alexander, C.M.O'D., Hauri, E.H., Sarafian, A.R., Nittler, L.R., Wang, et al., 2021. Highly volatile element (H, C, F, Cl, S) abundances and H isotopic compositions in chondrules from carbonaceous and ordinary chondrites Geochim. Cosmochim. Acta, 301, 230-258.
Shimizu, K., Saal, A.E., Myers, C.E., Nagle, A.N., Hauri, E.H., Forsyth, D.W., Kamenetsky, V.S., Niu, Y., 2016. Two-component mantle melting-mixing model for

the generation of mid-ocean ridge basalts: Implications for the volatile content of the Pacific upper mantle. Geochim. Cosmochim. Acta 176, 44–80.
Shimizu, K., Ushikubo, T., Hamada, M., Itoh, S., Higashi, Y., Takahashi, E., et al., 2017. H_2O, CO_2, F, S, Cl, and P_2O_5 analyses of silicate glasses using SIMS: Report of volatile standard glasses. Geochem. J. 51 (4), 299–313.
Shishkina, T.A., Botcharnikov, R.E., Holtz, F., Almeev, R.R., Jazwa, A.M., Jakubiak, A.A., 2014. Compositional and pressure effects on the solubility of H_2O and CO_2 in mafic melts. Chemical Geology 388, 112–129.
Sides, I.R., Edmonds, M., Maclennan, J., Swanson, D.A., Houghton, B.F., 2014. Eruption style at Kīlauea Volcano in Hawai'i linked to primary melt composition. Nature Geosciences 7, 464–469.
Spilliaert, N., Allard, P., Métrich, N., Sobolev, A.V., 2006. Melt inclusion record of the conditions of ascent, degassing, and extrusion of volatile-rich alkali basalt during the powerful 2002 flank eruption of Mount Etna (Italy). J. Geophys. Res. 111, B04203.
Sun, C., Dasgupta, R., 2020. Thermobarometry of CO_2-rich, silica-undersaturated melts constrains cratonic lithosphere thinning through time in areas of kimberlitic magmatism. Earth Planet. Sci. Lett. 550, 116549.
Sun, C., Dasgupta, R., 2023. Carbon budget of Earth's deep mantle constrained by petrogenesis of silica-poor ocean island basalts. Earth and Planet. Sci. Lett. 611, 118135.
Sun, S.S., McDonough, W.F., 1989. Chemical and Isotopic Systematics of Oceanic Basalts: Implications for Mantle Composition and Processes. In: Saunders, A.D., Norry, M.J. (Eds.), Magmatism in the Ocean Basins, Geological Society, 42. Special Publications, London, pp. 313–345.
Taracsák, Z., Hartley, M.E., Burgess, R., Edmonds, M., Iddon, F., Longpré, M.-A., 2019. High fluxes of deep volatiles from ocean island volcanoes: Insights from El Hierro. Canary Islands. Geochim Cosmochim. Acta 258, 19–36.
Toplis, M.J., 2005. The thermodynamics of iron and magnesium partitioning between olivine and liquid: criteria for assessing and predicting equilibrium in natural and experimental systems. Contrib. Mineral. Petrol. 149, 22–39.
Torres, P., Silva, L.C., Munhá, J., Caldeira, R., Mata, J., Tassinari, C., 2010. Petrology and geochemistry of lavas from Sal Island: Implication for the variability of the Cape Verde magmatism. Comunicaçõe Geológicas 97, 35–62.
Tucker, J.M., Hauri, E.H., Pietruszka, A.J., Garcia, M.O., Marske, J.P., Trusdell, F.A., 2019. A high carbon content of the Hawaiian mantle from olivine-hosted melt inclusions. Geochim Cosmochim. Acta 254, 156–172.
Van Achterbergh, E., Ryan, C.G., Jackson, S.E., Griffin, W.L., 2001. Data reduction software for LA-ICP-MS. Laser-Ablation-ICPMS in the earth sciences—principles and applications Miner. Assoc. Can. (short Course Series) 29, 239–243.
Venugopal, S., Schiavi, F., Moune, S., Bolfan-Casanova, N., Druitt, T., William-Jones, G., 2020. Melt inclusion vapour bubbles: the hidden reservoir for major and volatile elements. Sci. Rep. 10, 9034.
Vigouroux, N., Wallace, P.J., Kent, A.J.R., 2008. Volatiles in High-K Magmas from the Western Trans-Mexican Volcanic Belt: Evidence for Fluid Fluxing and Extreme Enrichment of the Mantle Wedge by Subduction Processes. J. Petrol. 49, 1589–1618.
Wallace, P.J., 2005. Volatiles in subduction zone magmas: concentrations and fluxes based on melt inclusions and volcanic gas data. J. Volcanol. Geotherm. Res. 140, 217–240.
Wallace, P.J., Kamenetsky, V.S., Cervantes, P., 2015. Melt inclusion CO_2 contents, pressures of olivine crystallization, and the problem of shrinkage bubbles. Am. Mineral. 100, 787–794.
Wallace, P.J., Plan, T., Bodnar, R.J., Gaetani, G.A., Shea, T., 2021. Olivine-hosted melt inclusions: a microscopic perspective on a complex magmatic world. Annu. Rev. Earth Planet. Sci. 49, 465–494.
Wang, X., Chou, I.-M., Hu, W., Burruss, R.C., Sun, Q., Song, Y., 2011. Raman spectroscopic measurements of CO_2 density: Experimental calibration with high-pressure optical cell (HPOC) and fused silica capillary capsule (FSCC) with application to fluid inclusion observations. Geochim Cosmochim. Acta 75, 4080–4093.
Wanless, V.D., Behn, M.D., Shaw, A.M., Plank, T., 2014. Variations in melting dynamics and mantle compositions along the Eastern Volcanic Zone of the Gakkel Ridge: insights from olivine-hosted melt inclusions. Contrib. Mineral. Petrol. 167, 1005.
Weaver, B.L., 1991. The origin of ocean island basalt end-member compositions: trace element and isotopic constraints. Earth and Planet. Sci. Lett. 104, 381–397.
Webster, J.D., Baker, D.R., Aiuppa, A., 2018. Halogens in mafic and intermediate-silica content magmas. In: Harlov, D.E., Aranovich, L. (Eds.), The Role of Halogens in Terrestrial and Extraterrestrial Geochemical Processes: Surface, Crust, and Mantle. Springer International Publishing, Cham, pp. 307–430.
Webster, J.D., Rebbert, C.R., 2001. The geochemical signature of fluid-saturated magma determined from silicate melt inclusions in Ascension Island granite xenoliths. Geochim. Cosmochim. Acta 65, 123–136.
Wieser, P.E., Lamadrid, H., Maclennan, J., Edmonds, M., Matthews, S., Iacovino, K., et al., 2021. Reconstructing magma storage depths for the 2018 Kīlauean eruption from melt inclusion CO_2 contents: The importance of vapor bubbles. Geochem. Geophys. Geosyst. 22, e2020GC009364.
Willbold, M., Stracke, A., 2006. Trace element composition of mantle end-members: Implications for recycling of oceanic and upper and lower continental crust. Geochem. Geophys. Geosyst. 7, Q04004.
Zanon, V., Silva, R., Goulart, C., 2023. The crust-mantle transition beneath the Azores region (central-north Atlantic Ocean). Contrib. Mineral. Petrol 178 (8), 50.